



1-1-2016

CFD Simulation Of Erosion Rates In Electrical Submersible Pumps

S M Mahdi Mofidian

[How does access to this work benefit you? Let us know!](#)

Follow this and additional works at: <https://commons.und.edu/theses>

Recommended Citation

Mofidian, S M Mahdi, "CFD Simulation Of Erosion Rates In Electrical Submersible Pumps" (2016). *Theses and Dissertations*. 2047.

<https://commons.und.edu/theses/2047>

This Thesis is brought to you for free and open access by the Theses, Dissertations, and Senior Projects at UND Scholarly Commons. It has been accepted for inclusion in Theses and Dissertations by an authorized administrator of UND Scholarly Commons. For more information, please contact und.commons@library.und.edu.

**CFD SIMULATION OF EROSION RATES IN ELECTRICAL
SUBMERSIBLE PUMPS**

by

Seyed Mohammad Mahdi Mofidian

Bachelor of Science, University of Tehran, 2006

Master of Science, IUST University, 2011

A Thesis

Submitted to the Graduate Faculty

of the

University of North Dakota

in partial fulfillment of the requirements

for the degree of

Master of Science

Grand Forks, North Dakota

August

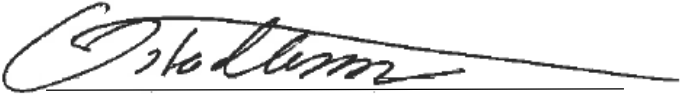
2016

© 2016 Seyed Mohammad Mahdi Mofidian

This thesis, submitted by Seyed Mohammad Mahdi Mofidian in partial fulfillment of the requirements for the Degree of Master of Science from the University of North Dakota, has been read by the Faculty Advisory Committee under whom the work has been done and is hereby approved.

 07.1.2016
Hadi Jabbari

Hadi Jabbari, Ph.D.



Mehdi Ostadhassan, Ph.D.



Minou Rabiei, Ph.D.

This thesis is being submitted by the appointed advisory committee as having met all of the requirements of the School of Graduate Studies at the University of North Dakota and is hereby approved.



Dr. Grant McGimpsey
Dean of the School of Graduate Studies

7/5/16
Date

PERMISSION

Title CFD simulation of erosion rates in Electrical Submersible Pumps
Department Sustainable Energy Engineering
Degree Master of Science

In presenting this thesis in partial fulfillment of the requirements for a graduate degree from the University of North Dakota, I agree that the library of this University shall make it freely available for inspection. I further agree that permission for extensive copying for scholarly purposes may be granted by the professor who supervised my thesis work or, in his absence, by the chairperson of the department or the dean of the School of Graduate Studies. It is understood that any copying or publication or other use of this thesis or part thereof for financial gain shall not be allowed without my written permission. It is also understood that due recognition shall be given to me and to the University of North Dakota in any scholarly use which may be made of any material in my thesis.

Seyed Mohammad Mahdi Mofidian
17 June 2016

TABLE OF CONTENTS

LIST OF FIGURES.....	vi
LIST OF TABLES.....	viii
ACKNOWLEDGMENTS.....	ix
ABSTRACT.....	x
CHAPTERS	
I. INTRODUCTION.....	1
II. LITERATURE REVIEW.....	9
III. METHODOLOGY.....	26
IV. RESULTS AND DISCUSSION.....	32
V. CONCLUSION AND RECOMMENDATION.....	51
REFERENCES.....	53

LIST OF FIGURES

Figure	Page
1. Comparison between different artificial methods	2
2. Usage of different types of artificial lift methods in U.S.	3
3. The Nomenclature of an impeller	5
4. Schematic of a multistage ESP pump	5
5. Sand problem in fixed impeller ESP	7
6. Schematic of the radial impeller's geometry.....	17
7. Schematics of the setup for the PIV system.....	23
8. Schematic of the impeller	32
9. Meshed model of the impeller	33
10. Mesh independency of the impeller	34
11. SIMPLE method flowchart	35
12. Pressure contour (psia) at 60 Hz, sand size and density as $53\mu\text{m}$ and 2300kg/m^3	38
13. Velocity magnitude (m/s) at 60 Hz, sand size and density as $53\mu\text{m}$ and 2300kg/m^3	38
14. Erosion rate [$\mu\text{m/hr}$] at 60 Hz, sand size and density as $53\mu\text{m}$ and 2300kg/m^3	39

15. Pressure contour (psia) at 60 Hz, sand size and density as 150 μm and 2300 kg/m^3	40
16. Velocity magnitude (m/s) at 60 Hz, sand size and density as 150 μm and 2300 kg/m^3	40
17. Erosion rate [$\mu\text{m}/\text{hr}$] at 60 Hz, sand size and density as 150 μm and 2300 kg/m^3	41
18. Pressure contour (psia) at 50 Hz, sand size and density as 53 μm and 2300 kg/m^3	41
19. Velocity magnitude (m/s) at 50 Hz, sand size and density as 53 μm and 2300 kg/m^3	42
20. Erosion rate [$\mu\text{m}/\text{hr}$] at 50 Hz, sand size and density as 53 μm and 2300 kg/m^3	42
21. Pressure contour (psia) at 50 Hz, sand size and density as 150 μm and 2300 kg/m^3	43
22. Velocity magnitude (m/s) at 50 Hz, sand size and density as 150 μm and 2300 kg/m^3	43
23. Erosion rate [$\mu\text{m}/\text{hr}$] at 50 Hz and sand size 150 μm and 2300 kg/m^3	44
24. Pressure contour (psia) at 50 Hz, sand size and density as 53 μm and 2100 kg/m^3	45
25. Velocity magnitude at 50 Hz, sand size and density as 53 μm and 2100 kg/m^3	45
26. Erosion rate [$\mu\text{m}/\text{hr}$] at 50 Hz, sand size and density as 53 μm and 2100 kg/m^3	46
27. Pressure contour (psia) at 60 Hz, sand size and density as 53 μm and 2300 kg/m^3	47
28. Velocity magnitude at 60 Hz, sand size and density as 53 μm and 2300 kg/m^3	47
29. Erosion rate [$\mu\text{m}/\text{hr}$] at 60 Hz, sand size and density as 53 μm and 2300 kg/m^3	48
30. Pressure contour (psia) at 50 Hz, sand size and density as 150 μm and 2300 kg/m^3	49
31. Velocity magnitude at 50 Hz, sand size and density as 150 μm and 2300 kg/m^3	49
32. Erosion rate [$\mu\text{m}/\text{hr}$] at 50 Hz, sand size and density as 150 μm and 2300 kg/m^3	50

LIST OF TABLES

Table	Page
1. Set ups and scheme used in the solution method	36
2. Common properties of working fluid	37

ACKNOWLEDGMENTS

I would like to start by thanking my committee members, Dr. Jabbari, Dr. Ostadhassan and Dr. Rabiei for their support and comments throughout the review of my thesis.

I would also like to thank my friend Dr. Sahand Pirouzpanah for all his helps.

Deeply from my heart with love and faith, I would like to thank my family for their encouragement.

Last but not least, I would like to thank God for all good deeds.

Dedicated to my beloved father for his measureless support from the Heaven, and my beloved

Mother

For her endless love, support and encouragement

ABSTRACT

Electrical Submersible Pump (ESP) is an efficient and useful artificial lift method for lifting fluids to the surface. In oil production, sand is an inevitable part which causes ESPs to fail regarding to erosion of the equipment. Therefore, erosion simulation in ESP pump would be a great help for maintenance and life span of the system. In the present work, a Computational Fluid Dynamics (CFD) simulation of erosion in an impeller is performed in order to give a better understanding. Meshing and CFD simulations are done using ANSYS Fluent software. Different scenarios are considered to find the effect of various parameters on the erosion rate. The pump is simulated at two frequencies as 50 and 60 Hertz. The model is based on Eulerian-Eulerian approach where the primary and secondary phases are oil and sand respectively. Also, CFD simulations of different boundary conditions, sand sizes and densities are presented to predict the erosion rate.

CHAPTER I

INTRODUCTION

In the early stages of the oil production, the bottomhole pressure is sufficient to overcome the head losses during the flow lifts up toward the surface. However, according to the diffusivity equation, the bottomhole pressure drops after a while to below the total pressure losses in the well. In such cases the artificial lifting methods are employed to increase the production rate. The most applicable artificial lift methods can be categorized into pump driven methods and gas lifting. The pump driven method subcategorizes into different major systems as positive-displacement plunger pump, Electrical Submersible Pump (ESP) or jet pumping. The classification of the pumps is based on the ways that fluid moves by forcing the fluid volume into the pump's discharge. In such way, displacing the fluid can be done by either rotating impeller, propeller/ rotor, or the positive displacement. Also, the rotating pumps can be classified into the radial, axial, or mixed flow groups according to the direction of the impeller's discharge.

As the name implies, in the radial flow impeller, fluid discharges radially with respect to the entrance. Likewise, the fluid enters and exists along the axis of rotation or the driving shaft in the axial flow pump. Due to the low head that happens in these pumps, they usually are used in large capacity applications such as, water supplies and irrigation [1]. In the mixed flow impeller, a combination of both radially and axially movements is expected, and the flow is subjected to the centrifugal force as well as the axial force. In these type of pumps, the fluid enters axially and discharges in both the axial and radial directions. Artificial lift method selection depends on the

actual field conditions, such as the well depth, production rates, fluid properties and the equipment where the pump should be installed on it. In Fig. 1, the recommended working condition of three most common methods is depicted.

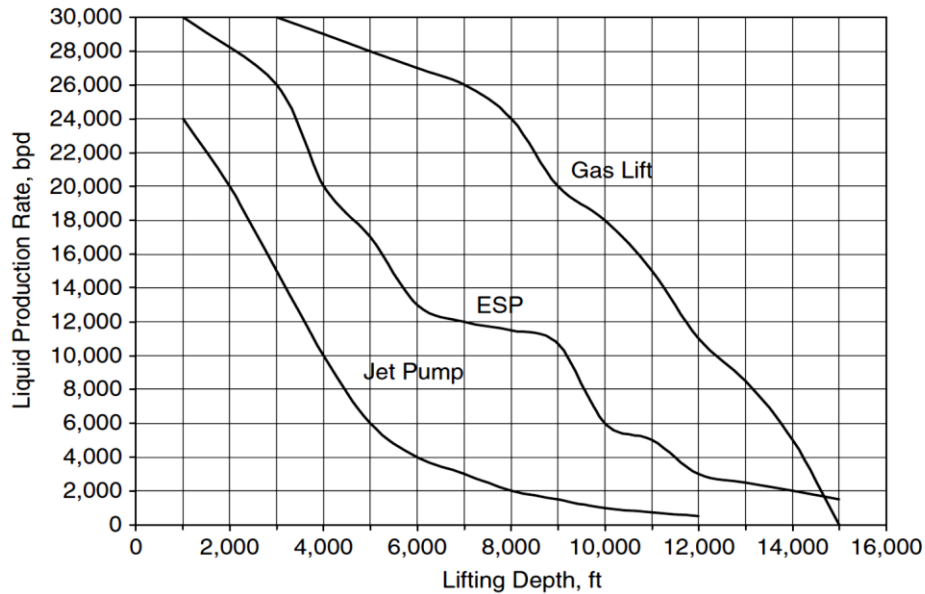


Figure 1. Comparison between different artificial methods [1]

In this figure, the production rate versus lifting depth for gas lifting, ESP and jet pumping methods are presented. Also, we can find the appropriate potential of ESP pumps for lifting the fluid within a wide range of depth and production rate in comparison with the other methods. Due to this potential, extensive research has been conducted for improving ESP pumps to introduce more efficient system with higher life span [1, 2]. Fig. 2 depicts the contribution of artificial lift methods in USA among about 500000 oil wells. It shows that various types of sucker-rod pumps are utilized on about 85 percent of the well and ESP pumps are applied in 4% of the wells [3].

In terms of maintenance, the costs for every overhaul of a failed ESP pump encourages the companies to have a more reliable unit with better design. Some of these expenses are related to setting up and down the equipment and the labor costs. However, the evaluation of any methods

or systems like ESP pumps, requires consideration of both the limitation and advantages.

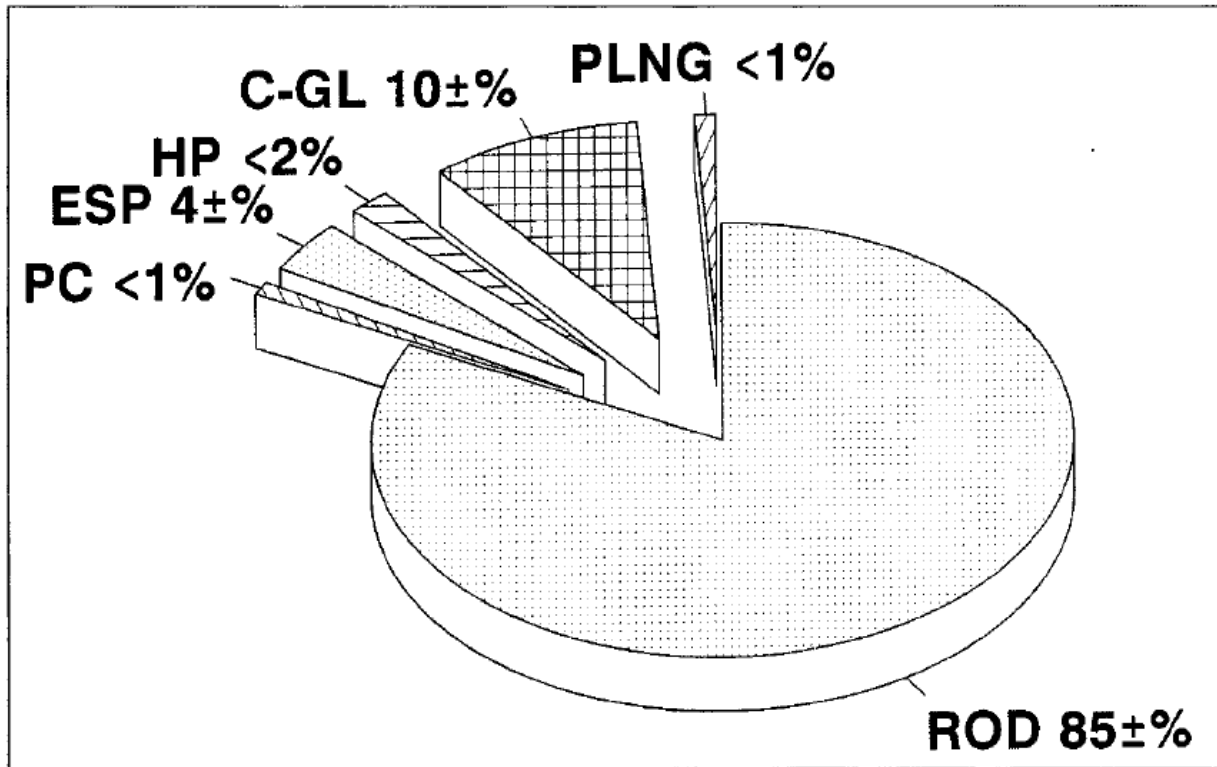


Figure 2. Usage of different types of artificial lift methods in U.S. [3]

For this purpose, some of the advantages and disadvantages of ESP unit are presented as follows:

Advantages:

- Requires minimal surface equipment
- Can work at high temperature
- Can produce high liquid volume
- Can be applied in deviated wells
- Can be installed in both offshore and surface environments
- Suitable for different well conditions

Disadvantages:

- Requires high initial capital cost

- Gas content deteriorates its efficiency
- Sand or other solid particles increase potentially system failure
- Maintenance difficulty
- Sensitivity to abrasive material
- Dependency to a reliable electrical power with high voltage source

As mentioned, the ESP pumps can be classified into the rotary pumps that widely are used by the oil and gas industry for artificial lift. ESP pumps contain these main parts:

- 1- Impeller
- 2- Casing
- 3- Diffuser

The rotating part of ESP is the impeller and it contains curved vanes which are connected to the shaft. It increases the kinetic energy of the fluid by transferring the work of the motor to the system and implementing a centrifugal force on the flow. It can be made of different materials such as iron, aluminum or plastic based on the transferring power or the pumps conditions. Based on its characteristics, it can be categorized into three different types: open impeller, enclosed impeller and semi-open impeller. The main components of any type of impellers usually are blade, hub and shroud, leading and trailing edges. Refer to Fig. 3, the nomenclature of the impeller parts and its construction is presented. [1]

The discharged flow of the impeller will have different eddy sizes which reduces the total energy due to interaction between impeller and eddies. The diffuser is a part of an ESP with the role of reducing this energy loss. In each ESP unit, multistage stack of impellers and diffusers in an ESP are shown in Fig. 4. In each stage there is an impeller to support the required energy to the system by taking from the pump shaft and the stationary part as diffuser to direct the outlet flow of the

previous impeller to the next stage impeller. At the inlet of each stage, the fluid from the previous stage enters the next impeller in an axial direction and increases its velocity at the discharge due to the rotational speed of the impeller's vanes. This process is repeated several times till the desired total pressure is gained.

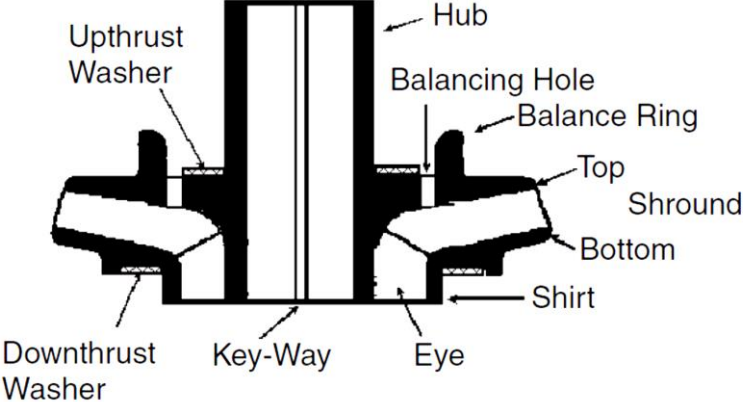


Figure 3. The Nomenclature of an impeller [2]



Figure 4. Schematic of a multistage ESP pump

The pump unit of an ESP usually operates in a vertical position, however the principle of operation remains the same when it is installed inclined. Generally, the producing capacity of an ESP pump

in each stages relates to the system characteristics as well as the operational conditions, such as:

- Rotational speed of the motor shaft
- Thermodynamic properties of the working fluid
- Design of the impeller
- Size of the impeller
- Actual required head of the pump

Maximum practical loaded stages by the ESP pump is limited by several factors, and each of them has an impact on the number of impellers and diffusers required. Some of these factors are:

- Mechanical strength of the motor shaft
- Maximum allowable load on the thrust bearing of the system
- The maximum burst-pressure rating of the pump housing

The frequency of the electrical submersible pumps is another factor which should be optimized in pumps that are working in a downhole environment. However, the relationships between the rotational speed and the performance parameters of the pump in different rotational speed rules by the affinity laws. Affinity laws consider the relationship between the performance parameters and rotational speed of a centrifugal pump. These rules can be expressed mathematically in following equations [1]:

$$Q_2 = Q_1 \left(\frac{N_2}{N_1} \right) \quad (1-1)$$

$$H_2 = H_1 \left(\frac{N_2}{N_1} \right)^2 \quad (1-2)$$

$$BHP_2 = BHP_1 \left(\frac{N_2}{N_1} \right)^2 \quad (1-3)$$

where N, Q, H and BHP are pump rotational speed, volume flow rate, pump Head and required brake horsepower respectively. Regarding to the above equations, the flow rate of a pump is directly proportional to the rotational speed. Also, pump head and brake horsepower change

proportionally to the square of the rotational speed.

One main problem we often face within ESPs is the erosion. Since impellers produce fluids from oil well usually contain solid particles, the erosion from such particles can affect the performance of an ESP and can cause failure of the unit and the moving parts of the pump. Hisham [2] investigated the most common failures in ESP pumps, and based on his study, cable and motor parts are the major components which need more maintenance during the life span of ESPs. Fig. 5 depicts the possible locations which are prone to sand erosion during the operation of ESPs [1].

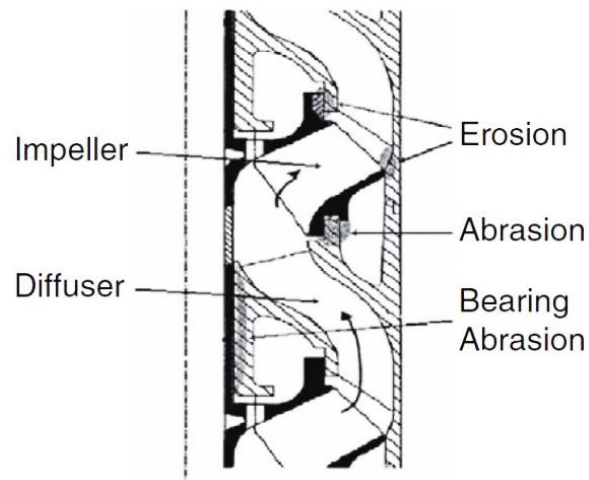


Figure 5. Sand problem in fixed impeller ESP [2]

The magnitude of erosion depends on hardness, concentration, size, shape, and toughness of solid particles. Moreover, the characteristics of sand production can be explained by the rock mechanics principles as follows [1]:

- Usually sand production starts at high flow rates
- After the breakthrough, sand production increases

It is worth to mention that the solids other than sand, such as iron sulfide and calcium carbonate may also cause erosion in a pump. However, most erosion problems arise from the production of

sand and reservoir fluids. There are some methods to extend the life span of ESP pumps which are subjected to sand erosion. For example, hardening of the surface through using hard materials such as silicon carbide, tungsten carbide and ceramic. However, hard materials are very brittle and they can fracture very easily if the loads reach to a certain value. Improving the design and manufacturing of ESPs can also help reducing the risk of erosion of pumps during the operation. Based on what was discussed, modeling and understanding the behavior of fluid inside the ESP pumps have been a great interest to many researchers. The investigations can have different approaches as numerical, experimental and analytical methods. With the numerical approach there have been conducted extensive research conducted on using CFD simulation to modeling the fluid flow in ESPs which is used in this project too. In this regards, the objective of the present thesis is stated in chapter two. Then, literature review is presented in chapter three and the approaches which are used to simulate erosion rate are covered in chapter four. Finally, the results are presented and discussed in chapter five and recommendations for the future studies are suggested in chapter six.

This project builds on previous work on using CFD simulation to model fluid behavior and erosion rate prediction in ESPs. The erosion problem in ESPs is a key that determines the life span of the pump. In this thesis, we discuss the CFD simulation using k-epsilon RANS turbulence model for predicting the erosion rates in ESPs. The analysis in this study is performed using ANSYS Fluent. Fluent was selected because of its capability to solve fluid flow equations efficiently. The simulation is performed to assess the effect of each parameter on erosion rate in ESPs. The result from this research will help pump manufacturers to have a prediction of the life span of their products, and help the consumers evaluate maintenance costs for ESPs.

CHAPTER II

LITERATURE REVIEW

Marsis et al. [4] studied the hydraulic thrust in an ESP pump which carries a mixed flow in the multistage pump and includes all the components and balance holes. They validated their results with experimental data. Their model was a transient analysis on the impeller types 338, 538 and 400 series which are designed and manufactured by Baker Hughes Inc. In case of the turbulence modeling, they applied the k-epsilon model. Three different scenarios for the number of the balance hole were considered and the results were compared to the actual tested thrust. The three scenarios were selected as zero, two and six balance hole, where the six balance hole shows the minimum thrust.

Hadjiyannis et al. [5] performed experimental testing and CFD modeling on the erosion study of vertical submersible pumps. The study focused on experimental approach for selection of the most proper coating materials which involve nano-indentations. The coating materials were selected as plasma and high velocity oxygen fuel (HVOF) which are cost effective solutions in the pump industry. They applied Finnie model to determine erosion rate in the impeller and diffuser. Finally, they obtained the velocity of particles and compared the computational results with the data from experimental tests. According to the Finnie Model, the key parameters are particles impact velocity, surface-particle collision angle and wall properties where the particles are colliding. The mathematical expression of Finnie Model is shown in the following equations:

$$E = kV_p^n f(\gamma) \quad (2-1)$$

$$f(\gamma) = \begin{cases} \frac{1}{3} \cos^2 \gamma & \tan \gamma > \frac{1}{3} \\ \sin(2\gamma) - 3 \sin^2 \gamma & \tan \gamma < \frac{1}{3} \end{cases} \quad (2-2)$$

where E, K, V_p and γ represent non-dimensional mass, erosion factor, local particle velocity and the impact angle respectively. Their results showed that the balanced combination of toughness and hardness is important for selecting a pump coating material. Perez et al. [6] utilized ANSYS® CFX to study the fluid flow in a centrifugal pump and compared the results with the experimental ones. The centrifugal pump used in the test is a commercial centrifugal pump with two stages, eight backward curved blades, and a twelve-vane diffuser. They used mass and momentum conservation equations to properly address the flow behavior in centrifugal pumps, which are:

$$\vec{\nabla} \cdot \vec{V}_{xyz} = 0 \quad (2-3)$$

$$-\frac{1}{\rho} \nabla p + \nu \nabla^2 \vec{V}_{xyz} + \vec{g} = 2\vec{\omega} \times \vec{V}_{xyz} + \vec{\omega} \times (\vec{\omega} \times \vec{r}) + \frac{d\vec{V}_{xyz}}{dt} + \vec{V}_{xyz} \cdot \vec{\nabla} V_{xyz} \quad (2-4)$$

The terms $2\vec{\omega} \times \vec{V}_{xyz}$ and $\vec{\omega} \times (\vec{\omega} \times \vec{r})$ are the Coriolis and centripetal accelerations, $\frac{1}{\rho} \nabla p$ is the pressure gradient, $\nu \nabla^2 \vec{V}_{xyz}$ is the viscosity dissipation and \vec{g} as gravity acceleration part. On the right hand side of the equation, there are the temporal acceleration and convective of the flow. Also, the rest of the nomenclatures are ρ , p , ν , \vec{V}_{xyz} , $\vec{\omega}$ and \vec{r} which respectively represent specific mass, hydrostatic pressure, kinetic viscosity, fluid velocity on a non-inertial reference framework system, angular velocity of the rotor, position of a particle to the origin of the non-inertial reference framework system. In order to obtain the turbulent flow, the Reynolds average equations, conservative of mass and momentum equations and the Boussinesq hypothesis were used. The applied equations are presented as below: [6]:

$$\frac{\partial \bar{u}}{\partial x} + \frac{\partial \bar{v}}{\partial y} + \frac{\partial \bar{w}}{\partial z} = 0 \quad (2-5)$$

$$\frac{\partial \bar{u}}{\partial t} + \frac{\partial \bar{u}\bar{u}}{\partial x} + \frac{\partial \bar{u}\bar{v}}{\partial y} + \frac{\partial \bar{u}\bar{w}}{\partial z} = -\frac{1}{\rho} \frac{\partial \bar{p}}{\partial x} + \frac{\partial}{\partial x} \left[(v + v_t) \left(2 \frac{\partial \bar{u}}{\partial x} \right) \right] + \frac{\partial}{\partial y} \left[(v + v_t) \left(2 \frac{\partial \bar{u}}{\partial y} + \frac{\partial \bar{v}}{\partial x} \right) \right] + \frac{\partial}{\partial z} \left[(v + v_t) \left(2 \frac{\partial \bar{u}}{\partial z} + \frac{\partial \bar{w}}{\partial x} \right) \right] + S_x \quad (2-6)$$

$$\frac{\partial \bar{v}}{\partial t} + \frac{\partial \bar{v}\bar{u}}{\partial x} + \frac{\partial \bar{v}\bar{v}}{\partial y} + \frac{\partial \bar{v}\bar{w}}{\partial z} = -\frac{1}{\rho} \frac{\partial \bar{p}}{\partial y} + \frac{\partial}{\partial y} \left[(v + v_t) \left(2 \frac{\partial \bar{v}}{\partial y} \right) \right] + \frac{\partial}{\partial x} \left[(v + v_t) \left(2 \frac{\partial \bar{u}}{\partial y} + \frac{\partial \bar{v}}{\partial x} \right) \right] + \frac{\partial}{\partial z} \left[(v + v_t) \left(2 \frac{\partial \bar{v}}{\partial z} + \frac{\partial \bar{w}}{\partial y} \right) \right] + S_y \quad (2-7)$$

$$\frac{\partial \bar{w}}{\partial t} + \frac{\partial \bar{w}\bar{u}}{\partial x} + \frac{\partial \bar{w}\bar{v}}{\partial y} + \frac{\partial \bar{w}\bar{w}}{\partial z} = -\frac{1}{\rho} \frac{\partial \bar{p}}{\partial z} + \frac{\partial}{\partial z} \left[(v + v_t) \left(2 \frac{\partial \bar{w}}{\partial z} \right) \right] + \frac{\partial}{\partial x} \left[(v + v_t) \left(2 \frac{\partial \bar{w}}{\partial x} + \frac{\partial \bar{u}}{\partial z} \right) \right] + \frac{\partial}{\partial y} \left[(v + v_t) \left(2 \frac{\partial \bar{w}}{\partial y} + \frac{\partial \bar{v}}{\partial z} \right) \right] \quad (2-8)$$

in presence of domain rotation, the angular velocity must be considered. In this case the source terms S_x and S_y which are dependent on the frame motion are subjected to the changes as described in the following equations:

$$S_x = -2\omega_z \bar{v} - \omega_z^2 x \quad (2-9)$$

$$S_y = -2\omega_z \bar{u} - \omega_z^2 y \quad (2-10)$$

also the turbulent kinetic viscosity v_t can be defined as:

$$v_t = \frac{c_\mu k^2}{\varepsilon} \quad (2-11)$$

This model proposes a relationship between the turbulent kinetic viscosity v_t with the turbulent kinetic energy k and the energy diffusion ratio ε . In the equation (2-11) the c_μ term is a constant coefficient in the k -epsilon turbulent model. Since in the turbulence modeling, we should solve the production and dissipation of eddies beside Navier-Stokes equations, the equations for eddies' production and dissipation rates, can be written as:

$$\frac{\partial k}{\partial t} + \frac{\partial uk}{\partial x} + \frac{\partial vk}{\partial y} + \frac{\partial wk}{\partial z} = D_k + P_k - k \quad (2-12)$$

$$\frac{\partial \varepsilon}{\partial t} + \frac{\partial u\varepsilon}{\partial x} + \frac{\partial v\varepsilon}{\partial y} + \frac{\partial w\varepsilon}{\partial z} = D_\varepsilon + \frac{\varepsilon}{k} (C_{\varepsilon 1} P_k - C_{\varepsilon 2} \varepsilon) \quad (2-13)$$

D_k and D_ε are diffusive terms for k and ε , P_k describe the production of k , also $C_{\varepsilon 1}$ and $C_{\varepsilon 2}$ are constants. Description of D_k , D_ε and P_k are defined in the below equations:

$$D_k = \frac{\partial}{\partial x} \left[\left(v + \frac{v_t}{\sigma_k} \right) \frac{\partial k}{\partial x} \right] + \frac{\partial}{\partial y} \left[\left(v + \frac{v_t}{\sigma_k} \right) \frac{\partial k}{\partial y} \right] + \frac{\partial}{\partial z} \left[\left(v + \frac{v_t}{\sigma_k} \right) \frac{\partial k}{\partial z} \right] \quad (2-14)$$

$$D_\varepsilon = \frac{\partial}{\partial x} \left[\left(v + \frac{v_t}{\sigma_\varepsilon} \right) \frac{\partial \varepsilon}{\partial x} \right] + \frac{\partial}{\partial y} \left[\left(v + \frac{v_t}{\sigma_\varepsilon} \right) \frac{\partial \varepsilon}{\partial y} \right] + \frac{\partial}{\partial z} \left[\left(v + \frac{v_t}{\sigma_\varepsilon} \right) \frac{\partial \varepsilon}{\partial z} \right] \quad (2-15)$$

$$P_k = v_t \left\{ \left(\frac{\partial \bar{u}}{\partial y} + \frac{\partial \bar{v}}{\partial x} \right)^2 + \left(\frac{\partial \bar{u}}{\partial z} + \frac{\partial \bar{w}}{\partial x} \right)^2 + \left(\frac{\partial \bar{v}}{\partial z} + \frac{\partial \bar{w}}{\partial y} \right)^2 + 2 \left[\left(\frac{\partial \bar{u}}{\partial x} \right)^2 + \left(\frac{\partial \bar{v}}{\partial y} \right)^2 + \left(\frac{\partial \bar{w}}{\partial z} \right)^2 \right] \right\} \quad (2-16)$$

where the coefficients in k -epsilon turbulence model are:

$$C_\mu = 0.09; \sigma_k = 1.00; \sigma_\varepsilon = 1.30; C_{\varepsilon 1} = 1.44; C_{\varepsilon 2} = 1.92 \quad (2-17)$$

The authors modeled a centrifugal pump which is working at three different angular velocities as 806, 1000 and 1150 rpm. In their study, the boundary condition for the inlet was set to 0 Pa and the constant mass flow rate as 10-20-30-40-50 m³/h at the outlet were selected. They obtained the pressure at different points and compared them with the experimental results by installing the pressure sensors at the same points and measured the pressure during a minute by averaging the obtained data at every seconds. Based on their results, the difference between the simulation and experiment is higher when the mass flow rate increases. Furthermore, the existence of recirculation and swirling flow causes more disagreement between the numerical and experimental results at the diffuser.

Marsis et al. [7] utilized two computational fluid dynamics erosion models to predict the erosion rate in the ESP pump. The first model is ERC-2003 and was proposed by Russell at 2003 based on his empirical study, and the second one is the ERC-2008 which is the modification of previous method by Russell that covers the low-velocity flow range. They deployed two different approaches as the discrete phase method and Eulerian-Eulerian granular model for simulating the interaction between the fluid phase and the erosion material. They also discussed the impact angle

function as a key factor in their model to match the CFD model with the experimental data. By this model, the first particle collision at positive impact angle with the wall creating a gouge on it, causes the other particles which are flowing parallel to the wall impact the surface and remove the material off of it. Essentially ERC-2008 model predicts more accurate erosion rate contours around the complex geometry. This model is described as [7]:

$$E = AV_p^n f(\theta) \quad (2-18)$$

where E , V_p and $f(\theta)$ respectively are mass of erosion loss/mass of particles impinging, particle velocity and the impact angle function. Also A and N are experimentally determined constants.

In the model, a single stage MVP G470 ESP pump is used with the flow rates of 20 and 25 KBPD and the rotating speed of 3600 rpm. In case of erosion model, both the discrete phase model (DPM) and Eulerian-Eulerian approach are utilized. The main difference between these two models is that DPM model consists of separate flow and particle iterations, but in the Eulerian-Eulerian method the fluid flow of the liquid and the granular phases are simulated at the same time. Due to this definition, Eulerian-Eulerian model would be a more precise approach in higher sand volume fraction. They compared both CFD models with the experimental results to demonstrate the accuracy of the simulation, where the sand size assumed 53 micrometers and the sand concentration was 1 pound of sand per 1000 bbl of the liquid.

Finally, they concluded the Eulerian method can capture the particles and predict the erosion rate more efficient than DPM model.

Barrios and Prado [8] empirically studied the two-phase flow inside an ESP pump to predict the operational conditions that lead to surging. For this purpose, a special high speed instrumentation was selected to acquire the visual flow dynamics and bubble sizes. The two-stage ESP prototype

pump is a GC6100 model made by centrilift pump. The modified prototype stage consists of an impeller, diffuser, hub and the pump inlet pipe, were built from Plexiglas as a transparent material to allow flow visualization inside the channels. To capture a better vision of what is happening inside ESP, they removed shroud and painted other parts. They performed three types of tests as: single phase, surging test and bubble diameter measurement test.

They also determined a dimensionless parameter to compare dynamic behavior of the fluid inside the pump in different rotational speeds. They introduced sauter mean diameter (SMD) as diameter of the bubble having the same volume to surface area ratio to demonstrate the bubble size change in the tests. The definition of the SMD is presented as:

$$SMD = \frac{\sum_{i=1}^N N_i \delta_i^3}{\sum_{i=1}^N N_i \delta_i^2} \quad (2-19)$$

where N_i is the number of the bubble and δ_i is the bubble diameter. They performed the tests at different flow rates, and operational angular speeds of 900, 1200, and 1500 rpm.

At the end, they reported observation of small recirculation close to the pressure side zone of the blades and presence of bigger bubble at higher gas void fractions inside the pump.

Maitelli et al. [9] used the k-epsilon turbulence model to simulate a three-dimensional flow inside a centrifugal pump. They considered three different conditions where in each of them the impeller rotates in angular velocity of 3500rpm. In the first condition, the blade length of impeller was same as the real model design, the second model conducted for the condition of real blades length in presence of both the impeller and diffuser, and in the third case the external radius of the impeller and diffuser increased by 4 mm. In terms of the boundary conditions, the pressure at inlet was set as 1 atm with variable mass flow at the outlet. They compared the CFD results with the experimental data of the pump and reported more deviation from the experimental results in case of smallest flow rate.

Sun and Prado [10] presented a new incompressible single-phase model for ESP's head pump. They considered the fractional and shock losses in their model. At the first step, they obtained the head in frictionless condition using the ordinary differential equation for the pressure as:

$$\frac{dp}{dr_{streamline}} = [-\rho_l \frac{\partial w}{\partial t} \frac{ds}{dr} + \rho_l \omega^2 r - \frac{\rho_l}{2} \frac{dw^2}{dr} + \rho_l g_s \frac{ds}{dr}] \quad (2-20)$$

so, the frictionless pressure in the steady state condition would be:

$$dp = [-\rho_l \omega^2 r dr - \rho_l \frac{dw^2}{dr} - \rho_l g_s ds] \quad (2-21)$$

in such condition, the frictionless pump head is equal to the impeller head, that means:

$$H_{stage} = \frac{V_2^2 - V_1^2}{2g} + \frac{U_2^2 - U_1^2}{2g} + \frac{W_2^2 - W_1^2}{2g} \quad (2-22)$$

that is similar to the Euler head, so finally they derived these equations for the frictionless pump head:

$$H_{stage} = \frac{U_2^2 - U_1^2}{g} + \frac{W_2 U_2 \cos \beta_2 - W_1 U_1 \cos \beta_1}{g} = \frac{\omega^2}{g} (r_2^2 - r_1^2) - \frac{Q_l \omega}{2\pi g H} \left(\frac{1}{\tan \beta_2} - \frac{1}{\tan \beta_1} \right) \quad (2-23)$$

where p is the pressure, ρ_l is density, w is the relative flow velocity between the fluids and the channel, s is the distance from the entrance tip of impeller or diffuser to certain location on the streamline, r is the location, g is the gravitational acceleration, ω is the angular velocity, and β is the geometric blade angle.

They also discussed the pressure distribution and head equation in the presence of the friction losses, and proposed an ordinary differential equation for ESP pump at the radial position r along the channel as:

$$dp = [-\rho_l \omega^2 r dr - \rho_l \frac{dw^2}{dr} + \left(\frac{dp}{dr} \right)_f dr - \rho_l g_s ds] \quad (2-24)$$

in the above equation, the friction term, $\left(\frac{dp}{dr} \right)_f$ can be obtained from:

$$\left(\frac{dp}{dr}\right)_f = \left(\frac{dp}{ds}\right)_f \left(\frac{ds}{dr}\right) \quad (2-25)$$

To relate the friction term of the pressure loss in the equation (2-25) to the friction factor, f , the following equation is used:

$$\left(\frac{dp}{dr}\right)_f = -f \frac{\rho}{d_H} \frac{W^2}{2} \quad (2-26)$$

The shock loss is the other term that should be considered in the total head loss and it can be calculated as:

$$\Delta p_{shock,l} = \rho_l g [a_{shock,base} Q_l^2 + b_{shock,base} \left(Q_l \frac{\omega_{impeller}}{\omega_{impeller,base}}\right) + c_{shock,base} \left(\frac{\omega_{impeller}}{\omega_{impeller,base}}\right)^2] \quad (2-27)$$

in this equation, the head loss was calculated on the base condition which is determined in a certain rotational speed, and the coefficients: $a_{shock,base}$, $b_{shock,base}$, $c_{shock,base}$ can be obtained from the following equation:

$$\Delta H_{shock,water} = a_{shock,base} Q_l^2 + b_{shock,base} Q_l + c_{shock,base} \quad (2-28)$$

when the friction and shock loss terms are considered, the equation for head increment in every stages would be as follow:

$$\Delta p_{stage} = p_{next-Eye} - p_{Eye} - \Delta p_{shock,l} \quad (2-29)$$

To have a better understanding about this calculations and nomenclatures, Fig. 6 is depicted as follow:

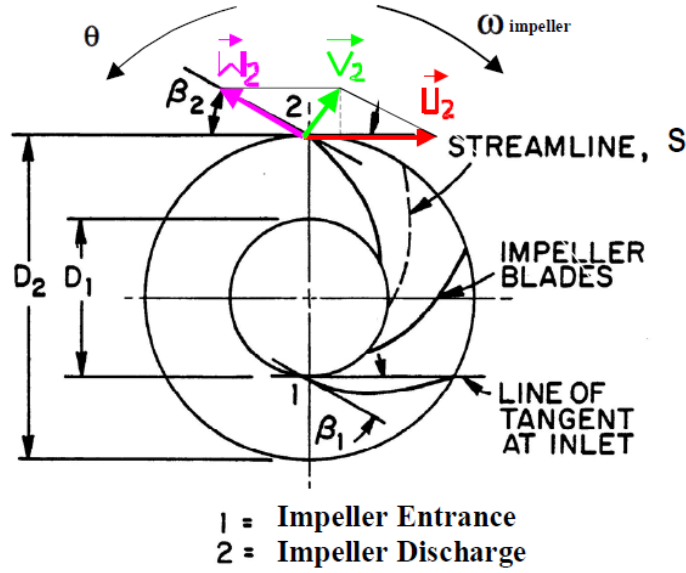


Figure 6. Schematic of the radial impeller's geometry [10]

Several investigations have studied the effect of the channel curvature, cross section shape, and rotational speed on the friction factor as the friction factor depends on the geometry, curvature, and the movement. In this paper [10], they defined different friction factor for the impeller and diffuser based on the critical Reynolds number, which it can be written as:

for the diffuser:

$$(N_{Re})_{crit_effect,diff.} = (N_{Re})_{crit_normal} \left(1 + \left(\frac{(N_{Re})_{crit,rectangular}}{(N_{Re})_{crit_normal}} + 1 \right) + \left(\frac{(N_{Re})_{crit,curved}}{(N_{Re})_{crit_normal}} - 1 \right) \right) \quad (2-30)$$

for the impeller:

$$(N_{Re})_{crit_effect,imp.} = (N_{Re})_{crit_normal} \left(1 + \left(\frac{(N_{Re})_{crit,rectangular}}{(N_{Re})_{crit_normal}} + 1 \right) + \left(\frac{(N_{Re})_{crit,curved}}{(N_{Re})_{crit_normal}} - 1 \right) + \left(\frac{(N_{Re})_{crit,rotation}}{(N_{Re})_{crit_normal}} - 1 \right) \right) \quad (2-31)$$

Finally, they used the multiplication factor to introduce the friction factor as:

$$f_{impeller} = F_{rectangular} F_{rotation} F_{curved} f_{circular, straight, rotation} \quad (2-32)$$

$$f_{impeller} = F_{rectangular} F_{rotation} F_{curved} f_{circular, straight, stationary} \quad (2-33)$$

Pak and Lee [11] simulated a centrifugal impeller containing five blades based on the k-epsilon turbulence method with the bubbly flow as the second phase flow. The model was a three-dimension geometry which employed the SIMPLE method to discrete the volume into the finite volumes subdomain. The working fluids were the water-air mixture with variable void fraction. In additions, the experimental tests were conducted to verify the CFD simulation results for both the void fraction and pressure distribution.

Gonzalez et al. [12] analyzed CFD model of a centrifugal pump with seven impeller blades and axial suction and volute casing, in order to find the rotor-stator interaction on it. They compared the experimental results with the obtained data from the simulation. The authors also used the pressure velocity coupling through the SIMPLER algorithm to perform a fluid structure interaction study on the blades of the rotor. Then, they presented the pressure fluctuation in the volute wall and compared it with the experimental data.

Feng et al. [13] investigated both the experimental and CFD analysis approaches of the fluid flow inside a radial diffuser pump. In the modeling part, they used three-dimensional Navier-Stokes equation with Detached Eddy Simulation (DES) turbulence model that was able to predict the flow field inside the pump. In the experimental test, the PIV visualization of the flow was performed where the pump was built from Plexiglas material to provide clear optical access for the camera to record the PIV measurement data. They observed the separation in the suction side of the impeller where the most turbulence zone is expected. They reported good agreement between their simulation and the experimental PIV data.

Zhou et al. [14] studied three different scenarios of centrifugal pumps. In the first scenario pump

has four straight blades (M_1), in the next one they considered the pump with six twisted blades (M_2). The last model was a centrifugal pump with six twisted blades but in a different sizes (M_3). They used of CFX software to solve three-dimensional Navier-Stokes equation combined with standard k-epsilon two-equation turbulence model. The boundary conditions were specified as constant mass flow at the inlet and two rotational speeds 2900 and 1450 rpm were used in the computations for all the cases. The results demonstrated that M_2 and M_3 designs were better than M_1 pump. Also, twisted blade models have higher pump efficiency compared to the straight blade geometry.

Asuaje et al. [15] analyzed an impeller and volute of a centrifugal pump. The model has a 3D geometry and CFX software was used to solve the problem. The authors utilized three types of turbulence model at the similar conditions as k-epsilon, k-omega and shear stress transport (SST) methods and compared their results together. Since the diffuser and impeller simulated together, the frozen-rotor interface was chosen to address the changes between the reference frame of the rotating impeller and static volute casing. In the frozen-rotor interface method, the relative position of the components would be updated step by step in a quasi-unsteady calculation. In terms of the boundary conditions, the inlet pressure was set to 1atm and the variable mass flow was specified at the outlet.

Thin et al. [16] simulated a single-stage centrifugal pump while water as a working fluid axially entered through the impeller eye and discharged radially. In the system, casing is designed to guide the fluid to the impeller, and converts the high kinetic energy related to the high velocity into the pressure term. Based on their design, an impeller with nine blades was analyzed. The flow rate of $0.179 \text{ m}^3/\text{s}$ with the rotor speed of 2900 rpm was set as the working conditions. To analyze the pump performance, they studied the effect of items as volute friction losses, shock losses, disk

friction losses, recirculation losses, and impeller friction losses of centrifugal pump.

Minggao et al. [17] analyzed a centrifugal pump based on the numerical approach. They performed a simulation in different rotational speed using ANSYS Fluent. In terms of the turbulence model, standard k-epsilon method was chosen with SIMPLEC algorithm. The simulation conducted as steady condition and moving reference frame was used to consider the impeller-volute interaction. The flow analysis results indicated that gradient of velocity has an important effect on the location and area of low pressure region of the blades. Furthermore, they cited Fluent software as an accurate and reliable commercial package for solving such kind of problems.

Zhou et al. [18] studied three-dimensional flow field inside a centrifugal pump. They deployed Solidworks software to create the volute casing and the flow passage. The working fluid assumed incompressible and viscous, so the flow is treated as three-dimensional incompressible turbulent flow. In this regard, three known turbulence methods of RNG k-epsilon Standard, Realizable k-epsilon and standard k-epsilon were utilized to simulate the flow field. The coupling equations of the pressure-velocity were calculated through the SIMPLE algorithm. In case of the frame rotation, Multiple Reference Frame (MRF) approach was applied for the numerical calculations. Boundary conditions were set as velocity at the inlet and mass flow at the outlet. The simulation results were compared with available experimental data, and it showed more accuracy for the RNG k-epsilon model. Moreover, they varied the number of blades to evaluate its effect on the efficiency of the pump.

Peri et al. [19] studied a CFD simulation on a choke to present the erosion rate of different parts as a function of flow rate and choke position. They cited numerous factors which affect the erosion rate, and discussed the interaction between all these factors which makes erosion reduction a challenging issue. They performed both the experimental and CFD modeling to validate their

work. They deployed the experimental data for validating the results of the CFD model. Based on the results, they proposed standard k-epsilon model as turbulence method which matches more closely to the experimental data. The sand with an average size of 300 microns was used in all the tests. They utilized the following formula for calculating the erosion rate [19]:

$$ER = AB^{-0.59}F(\theta)V^{1.73} \quad (2-34)$$

where ER is the erosion rate, A is an empirical constant, F is an empirical function that accounts for angle of impact, B is the Brinell hardness and V is the particle impact velocity. They concluded that the erosion rate increases in a quadratic fashion with respect to the flow rate.

Sirino and Morales [20] simulated a transient multi-stage model of ESP pump using CFX software. They considered the effect of different factors as flow rates, rotor speeds and fluid viscosity on ESP performance. They compared their results with the experimental data too. The geometry of the model was based on the semi-axial ESP pump with seven blades for impeller and seven vanes for diffuser. In case of boundary conditions, they assumed the walls as a smooth and no-slip condition, also the fixed static pressure, $P_{ref} = 0$, at the inlet and the fixed flow rate at the outlet were chosen. They introduced three dimensionless numbers to demonstrate the head and flow rate degradation in terms of viscosity and rotation speed. Finally, they proposed further studies are required since they were uncertain about the verification of their study in other cases.

Stel et al. [21] performed a CFD analysis of the flow in the first stage of a two-stage centrifugal pump with a vane diffuser. The authors aimed to study the unsteady flow caused by impeller-diffuser interaction. In this regards, different volumetric flow rates and variable rotor speeds were considered to present a wide range of designs. In addition, the first stage performance of the pump was compared with experimental data. They showed several large recirculation zones in both the impeller and diffuser notably tend to be concentrated near the blade pressure side. The authors

introduced a dimensionless flow coefficient to obtain the effect of rotor speed on the results as:

$$\phi = Q/(2\pi R^2 b \omega) \quad (2-35)$$

Where Q is the volumetric flow rate, R is the first impeller outlet radius, b is the blade height for the first impeller outlet and ω is the angular speed.

Muttalli et al. [22] modeled a centrifugal pump with ten blades impeller domain using ANSYS CFX in order to simulate the cavitation inside it. The authors assumed steady state conditions, constant fluid properties, incompressible fluid flow and the smooth walls during the simulation. In case of the boundary conditions, they set the constant pressure at the inlet and defined variable mass flow rate at the outlet. The standard k-epsilon model was used as turbulence model, where the impeller was rotating at different speeds 7000, 7700, 8400 and 9100 rpm with variable mass flow rates. They also studied the velocity contours to find the kinetic energy and dynamic pressure in the impeller.

Duasting et al. [23] conducted an experimental study at Schlumberger Ground Research (SGR) center to investigate the internal flows in ESP geometry using optical measurement techniques such as Particle Image Velocimetry (PIV) and Laser Doppler Velocimetry. In the Laser Doppler Velocimetry (LDV), velocity of individual particle tracers by measuring the Doppler frequency shift which would happen when a particle crossing an interference. For this purpose, they fabricated a transparent model of ESP pump from poly methyl methacrylate (PMMA) material. As they reported, the PIV system consisted of a dual cavity laser, optics, seeding particles, CCD camera, timing unit and related software. As it can be seen in Fig. 7, the laser beam was directed to the transport model through a laser light guide and a PIV camera was mounted above the set up. To synchronize the laser and camera, they utilized a timing card that is controlled by the PIV software. Also, data acquisition triggered by the motor controller and then an encoder which was

installed on the motor. They used highly reflective particles due to their better signal to noise ratio which made it more convenient for PIV system to trace the particles. However, they mentioned that by all the equipment and considerations, the noise of the other parts could not be eliminated completely. To measure both the axial and tangential velocities in the stage, they utilized a two-component LDV system. So, every second the measurements in the x and y directions were represented by a vector which is plotted for the graphical clarity and shown in the following figure.

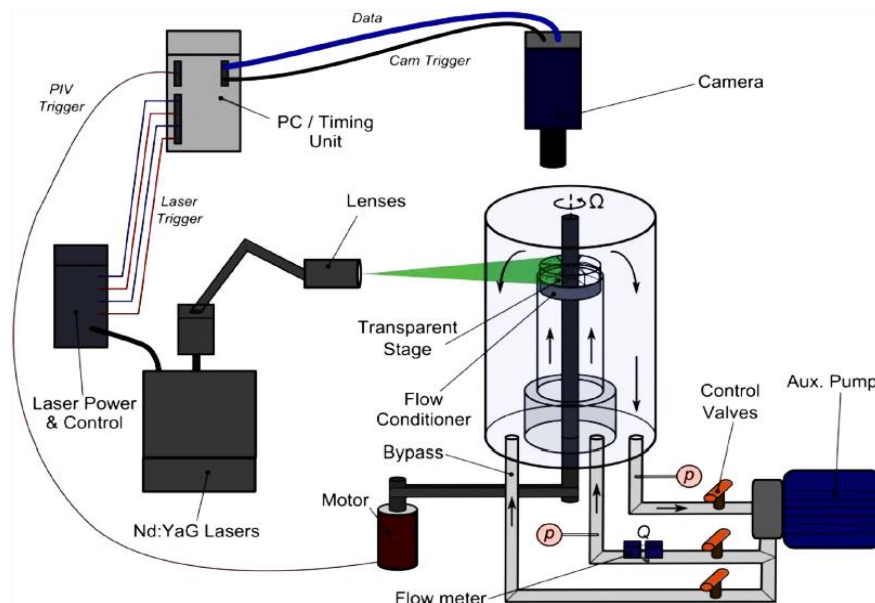


Figure 7. Schematics of the setup for the PIV system [23]

They demonstrated that the changes in Reynolds number can affect boundary region characteristics. As an example, they showed the thinner boundary region appears at the higher Reynolds numbers. They finally concluded that the optical measurement techniques can capture the recirculation and the wake regions in complex geometries like the pumps which experience the strong velocity fluctuation.

Caridad et al. [24] studied the simulation of the air-water mixture in an impeller of ESP pump and finally they compared their results with the experimental data. They considered the distribution of

the gas void fraction and the bubble size on the system. The standard k-epsilon turbulence model was chosen to simulate the fluid flow of two phase model. In case of boundary conditions, they specified the pressure at the inlet, and constant mass flow rate condition at the outlet. The results demonstrated gas pocket in the pressure side of the blade, and they related it to the drag and pressure gradient forces inside the impeller. This means that the drag force tends to push the bubble toward the outlet due to the slippage between two phases, and the pressure gradient force tends to slow it down. The authors studied three different gas void fractions with variable bubble diameters to figure out their effects on the flow field. They also concluded that the degradation of the pump's head in their model is related to the diameter of the bubbles. So, the balance between drag and pressure gradient forces can change the volume of the bubble.

Galavo et al. [25] performed a CFD simulation to determine the temperature distribution in the motor housing and evaluated heat transfer between ESP components and the environment. They validated the results by comparing CFD simulations with the field data obtained from wells equipped with bottom-hole sensors. Modeling was accomplished based on a single and multiphase flow. They applied Newton's law of cooling and calculated the convective heat transfer coefficient for both the laminar and turbulent regimes. In the mathematical approach, they calculated the temperature distribution by considering three components which were geothermal gradient temperature, motor temperature contribution and the fluid temperature.

Bellary et al. [26] introduced an evolutionary genetic algorithm to find the optimal point for an electrical submersible pump. The process included simulation of an impeller and implementing the optimization method on it with the objective function as efficiency and head maximization. They sketched the domain using Ansys Bladegen and Turbogrid modules and utilized ANSYS CFX for simulation, with the boundary condition as mass flow rate at the outlet and the rotor speed

3000 rpm. They considered some parameters which have more effects on the pump performance and then applied optimization strategies on them.

Marsis et al. [27] studied CFD modeling of an ESP pump manufactured by Baker Hughes which could handle up to 70% gas volume fraction. The computational results were compared with the experimental data at different diffuser geometry scenarios. The boundary conditions were defined as mass flow rate at the inlet and pressure at the outlet. They applied moving reference frame and moving mesh methods to simulate the impeller rotation. Based on their results, momentum of the flow increases by either increasing the rotor speed or mass flow rate in the pump.

Moreover, they showed the flow pattern at the diffuser outlet was non-homogenous and had strong vortices which increased head loss in the next impeller stage. They proposed the reduction of the separation in the diffuser in order to increase the efficiency of the impeller at the next stage. Finally, they reported the reduction of separation was enabled by modifying meridional profile, increasing the number of the blades and adding nozzle-shaped slot to the geometry.

CHAPTER III

METHODOLOGY

In order to simulate a three dimensional impeller, the k-epsilon turbulence model was utilized due to its ability to handle the transient turbomachinery problems. The k-epsilon model can be derived from the Reynolds-Averaged Navier-Stokes equation. It is based on transport equations for the turbulence kinetic energy (k) and its dissipation rate (epsilon). The Reynolds averaged Navier-Stokes is based on the continuity and momentum equations which can be written as follows:

$$\frac{\partial \rho}{\partial t} + \frac{\partial}{\partial x_i} (\rho \bar{u}_i) = 0 \quad (3-1)$$

$$\frac{\partial}{\partial t} (\rho \bar{u}_i) + \frac{\partial}{\partial x_j} (\bar{u}_i \bar{u}_j) = -\frac{\partial \bar{p}}{\partial x_i} + \frac{\partial}{\partial x_j} \left[\mu \left(\frac{\partial u_i}{\partial x_j} + \frac{\partial u_j}{\partial x_i} - \frac{2}{3} \delta_{ij} \frac{\partial u_l}{\partial x_l} \right) \right] + \frac{\partial}{\partial x_j} (-\rho \overline{u_i' u_j'}) \quad (3-2)$$

The last term of the equation (3-2) which is the Reynolds shear stress relates to the mean velocity gradient. This extra term in the average momentum can be defined as:

$$-\rho \overline{u_i' u_j'} = \mu_t \left(\frac{\partial u_i}{\partial x_j} + \frac{\partial u_j}{\partial x_i} \right) - \frac{2}{3} (\rho k + \mu_t \frac{\partial u_k}{\partial x_k}) \delta_{ij} \quad (3-3)$$

Where the turbulence kinetic energy, k, and its rate of dissipation, epsilon, can be obtained from the following transport equations:

$$\frac{\partial}{\partial t} (\rho k) + \frac{\partial}{\partial x_i} (\rho k u_i) = \frac{\partial}{\partial x_j} \left[\left(\mu + \frac{\mu_t}{\sigma_k} \right) \frac{\partial k}{\partial x_j} \right] + P_k + P_b - \rho \epsilon - Y_M + S_k \quad (3-4)$$

$$\frac{\partial}{\partial t} (\rho \epsilon) + \frac{\partial}{\partial x_i} (\rho \epsilon u_i) = \frac{\partial}{\partial x_j} \left[\left(\mu + \frac{\mu_t}{\sigma_\epsilon} \right) \frac{\partial \epsilon}{\partial x_j} \right] + \frac{\epsilon}{k} C_{\epsilon 1} (P_k + C_{\epsilon 3} P_b) - C_{\epsilon 2} \rho \frac{\epsilon^2}{k} + S_\epsilon \quad (3-5)$$

In these equations, P_k represents the generation of the turbulent kinetic energy due to the mean velocity gradient which is calculated in the equation (3-6), also, P_b is the generation of the turbulence kinetic energy regarding to the buoyancy which can be calculated as described in the

equation (3-9). In these equations, the turbulence viscosity term, μ_t , disappears. Where the viscosity depends only on the physical properties of the fluid, the turbulent viscosity is turbulent eddy viscosity which considers the effect of the velocity fluctuation. The turbulent viscosity formula can be written as:

$$\mu_t = \rho C_\mu \frac{k^2}{\varepsilon} \quad (3-6)$$

also, s is modulus of the mean rate of strain tensor and defined as:

$$s = \sqrt{2S_{ij}S_{ij}} \quad (3-7)$$

$$P_k = \mu_t S^2 \quad (3-8)$$

$$P_b = \beta g_i \frac{\mu_t}{Pr_t} \frac{\partial T}{\partial x_i} \quad (3-9)$$

in the equation (3-9), Pr_t is the Prandtl number for energy, g_i is the gravity and β is the coefficient of thermal expansion given by:

$$\beta = -\frac{1}{\rho} \left(\frac{\partial \rho}{\partial T} \right)_p \quad (3-10)$$

The constants for the k-epsilon model are as follows:

$$C_\mu = 0.09; \sigma_k = 1.0; \sigma_\varepsilon = 1.3; C_{\varepsilon 1} = 1.44; C_{\varepsilon 2} = 1.92 \quad (3-11)$$

To simulate the effect of the sand on the flow, we utilized the Eulerian-Granular (E-G) model to have the effect of the sands on the impeller. In the E-G model, the conservation of the momentum for the solid phase is derived as:

$$\frac{\partial}{\partial t} (\alpha_s \rho_s \vec{u}_s) + \nabla \cdot (\alpha_s \rho_s \vec{u}_s \vec{u}_s) = -\alpha_s \nabla p - \nabla p_s + \nabla \cdot \bar{\tau}_s + \alpha_s \rho_s \vec{g} + \alpha_s \rho_s (\sum F_n) + \sum_{l=1}^n (K_{sl} (\vec{u}_l - \vec{u}_s) + \dot{m}_{ls} \vec{u}_{ls}) \quad (3-12)$$

Here, p_s is the solid pressure, \dot{m}_{ls} is the mass transfer from the liquid to solid phase, \vec{g} relates to the gravity acceleration, $\sum F_n$ represents the external forces on the solid phase such as lift, virtual mass, drag and buoyancy forces.

Also, K_{sl} is the momentum exchange coefficient between the solid and fluid phases, and n is the total number of the phases.

The fluid-solid exchange coefficient can be written as the form:

$$K_{sl} = \frac{\alpha_s \rho_s f}{\tau_s} \quad (3-13)$$

where τ_s is the particulate relaxation time defined as:

$$\tau_s = \frac{\rho_s d_s^2}{18\mu_l} \quad (3-14)$$

In this equation d_s is the diameter of the particles. Also, in the equation (3-13) f represents the drag effect. Based on the Syamlal-O'Brien model, it can be defined as [28]:

$$f = \frac{C_D Re_s \alpha_l}{24v_{r,s}^2} \quad (3-15)$$

where C_D is the drag function, the subscribe l is for the liquid phase and s denotes the solid phase.

The solid phase Reynolds number, Re_s , is given as:

$$Re_s = \frac{\rho_l d_s |\vec{v}_s - \vec{v}_l|}{\mu_l} \quad (3-16)$$

If the equations (3-13) through (3-16) are combined together, the fluid-solid exchange coefficient has the following form:

$$K_{sl} = \frac{3\alpha_s \alpha_l \rho_l f}{4v_{r,s}^2 d_s} C_D \left(\frac{Re_s}{v_{r,s}} \right) |\vec{v}_s - \vec{v}_l| \quad (3-17)$$

During the trajectory of the particle in the continuous phase, external forces will act on it which makes the particle path. To take into account these forces, the general equation would be Newton's second law. If we consider the spherical particle with diameter d_p and the density ρ_p , so the mass of the particle would be as [29]:

$$m_s = \frac{1}{6} \rho_s \pi d_s^3 \quad (3-18)$$

To define the particle's velocity and the corresponding acceleration, the following formula would be used:

$$\dot{u}_s = \ddot{X}_s \quad (3-19)$$

where the calculation of the particle motion in the Lagrangian frame is based on the Newton's second law as:

$$m_s \dot{u}_s = \sum F_n \quad (3-20)$$

In the equation (3-20), right hand side term, $\sum F_n$, is the summation of the external forces on the particle which can be due to the other particles or the continuous phase, and the components of the forces include drag, buoyancy, virtual mass, lift, pressure and stress gradient[29]. Generally, drag force can be written as:

$$F_D = -m_p \frac{u_s - u_l}{\tau_p} \quad (3-21)$$

In the above equation, it is obvious that the source of drag force comes from the velocity difference between the particle and the continuous phase, where the τ_p represents the relaxation factor of the viscous drag and defined as [29]:

$$\tau_p = \frac{4}{3} \frac{\rho_s d_s}{\rho C_D |u_s - u_l|} \quad (3-22)$$

in the equation (3-22), the drag coefficient, C_D , depends on the flow regime around the discrete particle and should be calculated based on the relative particle Reynolds number. In this regards, using the Schiller-Naumann approximation, it can be derived [30]:

$$C_D = \begin{cases} \frac{24}{Re_p} & Re_p \leq 0.1 \\ \frac{24}{Re_p} (1 + 0.15 Re_p^{0.687}) & 0.1 \leq Re_p \leq 10^3 \\ 0.44 & Re_p \geq 10^3 \end{cases} \quad (3-23)$$

The other term in the external forces would be buoyancy force which is defined as:

$$F_B = \frac{1}{6} \pi d_s^3 g (\rho_s - \rho_l) \quad (3-24)$$

Based on this equation, when the diameter of the particle increases, the buoyancy force would have more impact on the particle trajectory.

The other force term can be the virtual mass force due to acceleration of the fluid mass near the particle, the formula for the virtual mass force would be as:

$$F_V = \frac{1}{12} \rho \pi d_p^3 \frac{d}{dt} (u_l - u_s) \quad (3-25)$$

The lift force acting on the particle is the external force due to velocity gradient in the primary phase flow field. This term is more significant when the diameter of the particles is considerable.

Generally, the lift force is computed from the following equation:

$$F_L = -0.5 \rho_l \alpha_l |\vec{u}_s - \vec{u}_l| \times (\nabla \times \vec{u}_l) \quad (3-26)$$

In most cases, the lift force term is not significant compared to the other forces, unless the particles diameter is considerable.

From the equations (3-21)-(3-26) we can define the external forces which act on the particles.

These forces come from other particles or the continuous flow. After considering all the forces in the momentum equation of solid phase, ANSYS Fluent uses stochastic tracking methods to predict the trajectory of the particles regarding to the turbulence nature of the flow. It means, Fluent will predict the trajectory of particles using the mean fluid phase velocity, \bar{u} , and applies the fluctuation velocity as:

$$u = \bar{u} + u' \quad (3-27)$$

Fluent uses the integral time scale concept, T , to predict the particle dispersion. Integral time scale demonstrates the time spent in turbulent motion along the particle path (ds) as [32]:

$$T = \int_0^\infty \frac{u_p'(t)u_p'(t+s)}{u_p'^2} ds \quad (3-28)$$

As it can be seen from the equation (3-28), integral time is proportional to the particle dispersion rate, which it means the larger values indicates more turbulence motion in the flow.

For simulation process, the first step to implement would be importing the computer-aided design (CAD) model of the pump. After importing the CAD file, we should discretize the model into

smaller elements which is called meshing and specify the boundary conditions. As a general rule, the boundary conditions should be physically meaningful such as specified pressure conditions or flow rate at the inlet or outlet. Also, it should be noted that the pressure and velocity boundary condition cannot be used at the same boundary since the velocity itself is influenced by the pressure gradient. After that, the turbulent kinetic energy and its dissipation rate can be calculated based on the value of turbulence intensity specified in the inlet. The last part of the simulation is the post processing step, which provides visualized results through the cutting planes, contouring, streamlines.

In terms of predicting the erosion rate, a new model which was proposed by Pirouzpanah et al. [33] is utilized. In their study, the erosion factor introduced as:

$$EF = (\alpha_s)^{0.08} \left(\frac{V_s}{\bar{V}_{s0}}\right)^{0.07} \left(\frac{K_f}{\bar{K}_{f0}}\right)^{1.25} \quad (3-29)$$

where EF is the erosion factor, α_s is the sand volume fraction, V_s and \bar{V}_{s0} are the near wall sand velocity and reference sand velocity, K_f and \bar{K}_{f0} are the turbulent kinetic energy and reference turbulent kinetic energy. Then, the erosion rate is calculated by following equation:

$$ER = A.EF^2 + B.EF \quad (3-30)$$

where ER is the erosion rate, A=0.0163 and B=0.8774 [33].

CHAPTER IV

RESULTS AND DISCUSSION

To solve the equations discussed in chapter three for an impeller, computational fluid dynamics (CFD) method is used in this research. CFD analysis uses numerical methods and algorithms to discretize the domain into small subdomains. Due to the great advantages of this method, CFD has become a useful tool in the research and industrial processes. In this chapter, we present the results of erosion rates simulation in an impeller under different operating conditions. As a first step to perform the numerical simulation, geometry of the impeller should be defined. For this purpose, we used Solidworks software that is capable to generate CAD files which were then imported into ANSYS Fluent. The CAD model of the impeller is illustrated in Fig. 8.

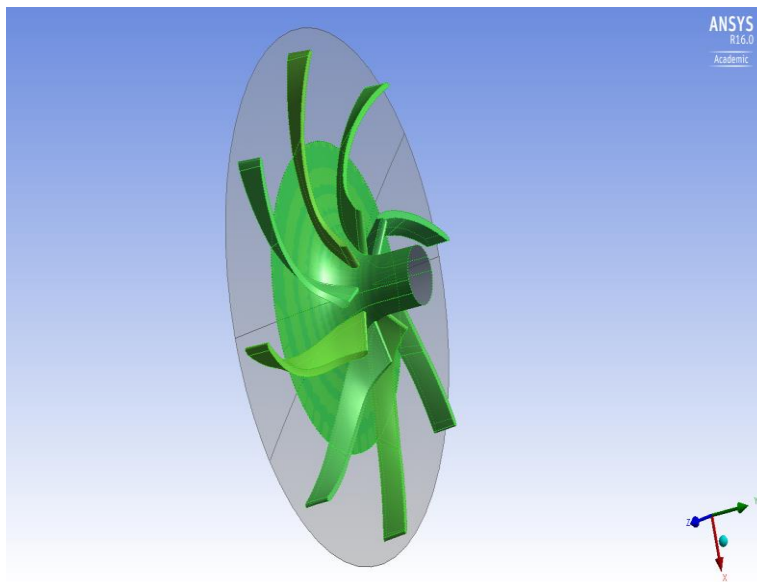


Figure 8. Schematic of the impeller

Analytical solution of a partial differential equation (PDE) in many cases is not applicable. In such conditions, the continuous domain of the problem is discretized into finite elements/volumes and numerical techniques are used to solve the problem. Regarding to the discretization technique, there are approaches as finite volume, finite element or finite difference methods. In this thesis ANSYS Fluent is used for solving the problem which is based on the finite volume method and considers the momentum and mass conservation at each finite volume level. So, the domain should be meshed after creating the geometry. Mesh generation or gridding is the process in which the domain of the problem is subdivided into small elements/volumes. More accurate results will be obtained when the domain is subdivided into more elements/volumes, called finer mesh. However, we should consider that the finer mesh needs more computational time and processing capability. To obtain an accurate solution with minimum possible computational time, the geometry should be meshed to a point that making finer mesh beyond it would have negligible impact on the results but the computational time increases. In terms of gridding, the model was meshed in ANSYS ICEM module that is shown in Fig. 9.

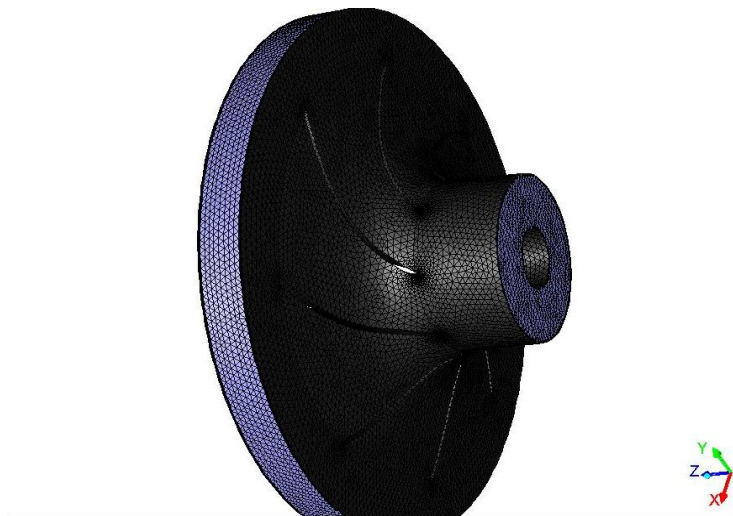


Figure 9. Meshed model of the impeller

Impeller's total pressure was used to check the mesh independency as it can be seen in Fig. 10. Since the pressure is specified at the outlet boundary condition, the accuracy of the pressure in the impeller is demanded and we used the total pressure criteria to find the optimum mesh of the domain. In this figure, the total pressure in different mesh numbers are compared with the result of the model with the largest mesh number and the differences are calculated as a percentage from this value.

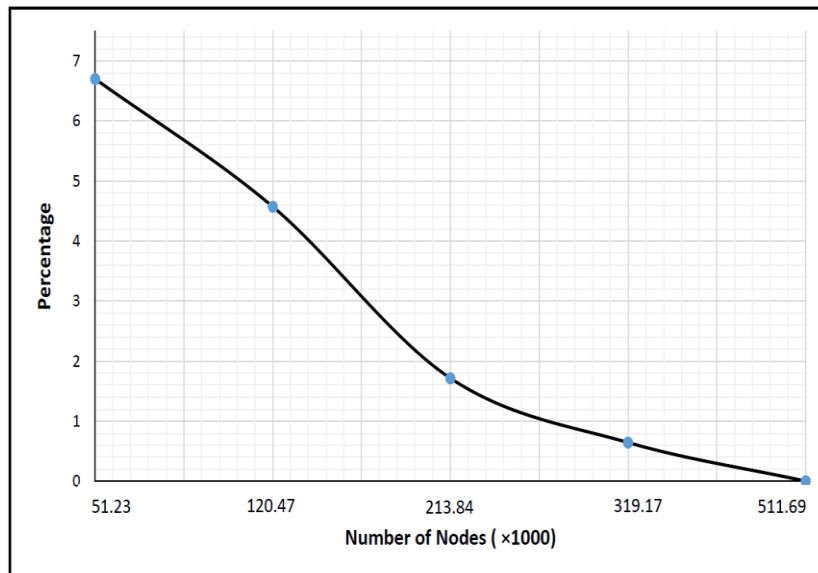


Figure 10. Mesh independency of the impeller

Therefore, in order to save the computational time with desired precision, the impeller was meshed with 319.17 K meshes, which its deviation from the highest mesh number is less than one percent. In terms of solving, the model was analyzed based on the standard k-epsilon two-equation turbulence model with SIMPLE algorithm where the algorithm flowchart is depicted in Fig. 11. Also, we used the moving reference frame model to present the rotational speed of the impeller that assumed as 3600 and 3000 rpm. All the other set up which applied in the solution are listed in table1. To have more stability on the model, Green-Gauss Node Based scheme was applied as gradient discretization method.

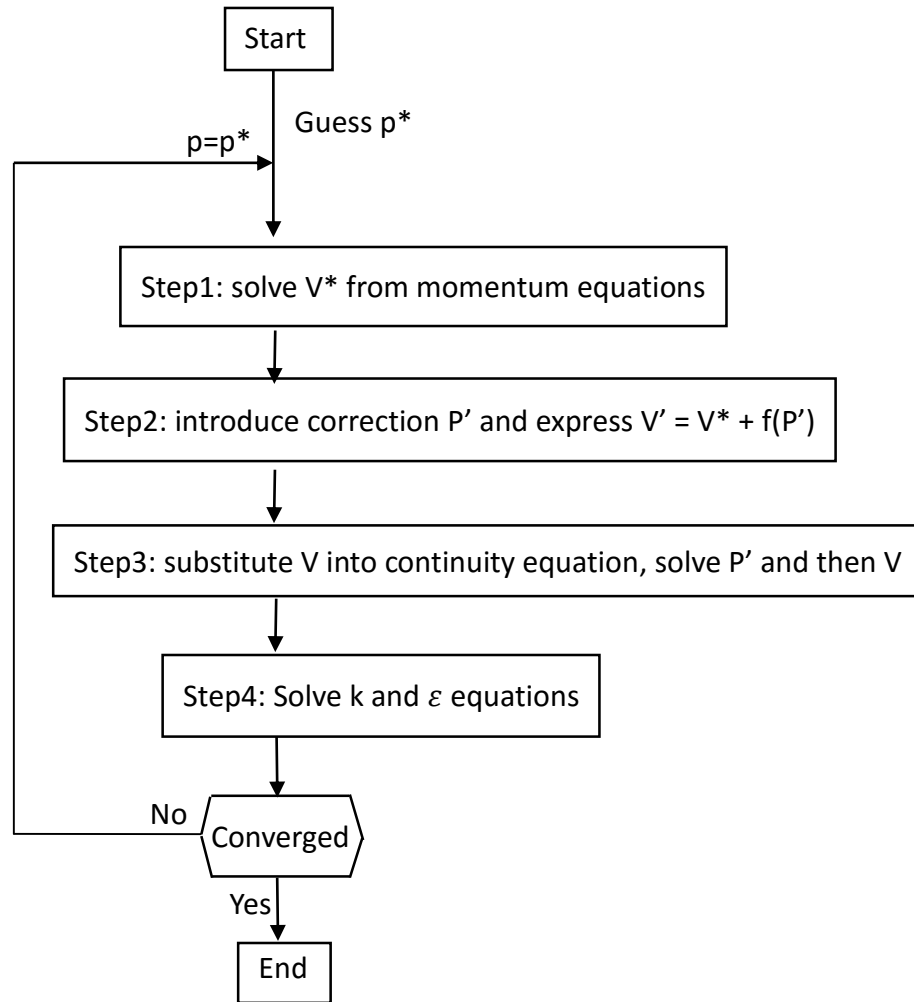


Figure 11. SIMPLE method flowchart [34]

Based on SIMPLE flowchart, solver starts with setting the boundary conditions, then solves the discretized momentum equation based on a pressure value conjecture to compute the intermediate velocity field. In step two, the pressure correction equation is solved then the pressure and velocity values will be updated. In the next step, these values are implemented into k-epsilon turbulence equations. This loop would be repeated till the solution converges.

To simulate two-phase flow, the Eulerian-Eulerian model was applied. Generally, there are two approaches as Euler-Lagrange (EL) and Euler-Euler (EE) models for CFD solving of multiphase problems. In EL method, the primary phase is treated as a continuous phase using Eulerian

framework, whereas the secondary phase is considered as discrete phase which follows by Newton's second laws of motion, like discrete particle modeling (DPM). This approach needs more computational memory in order to study the individual particle motion [35]. On the other hand, primary and secondary phases in EE method are considered as separate inter-penetrating fluids in the shared computational domain. So, the coupling between phases is obtained from pressure and interphase exchange coefficient. This model, allows the phases to stay in interaction together while treated separately, and the number of the particles is not limited.

Table1. Set ups and scheme used in the solution method

Model	k-epsilon standard
Scheme of the solution	Phase Coupled SIMPLE
Pressure Discretization	Second order
Momentum Discretization	Second order upwind
Turbulence kinetic energy Discretization	First order
Turbulence dissipation rate Discretization	First order

During the simulation, under relaxation factors for pressure, density, momentum, volume fraction, turbulent kinetic energy, turbulent dissipation rate and turbulent viscosity were chosen to be 0.2, 0.5, 0.35, 0.25, 0.4, 0.4 and 0.4 respectively. The working fluid is oil with the viscosity and specifications listed in table 2. The second phase also is sand with density varying from 2100 to 2300 kg/m³ [33].

Table 2. Common properties of working fluid

Working fluid	Oil
temperature	200°F
Viscosity	0.6cp
API gravity oil	35API
Impeller frequency	50 and 60 Hz

In the pre-processing step, one of the most important set up is related to the definition of the boundary conditions. It means that the behavior of a differential equation at the boundary of its domain will be defined by the boundary conditions. So, they are critical component of simulation and they should be specified appropriately. As a general rule, a physical meaningful boundary condition, such as a specified pressure condition, should be considered at the boundaries. Also, the pressure and velocity cannot be used at the same boundary since the velocity is influenced by pressure gradients as well. Therefore, the pressure defined at the outlet boundary condition and flow mass specified at the inlet in all the presented models in this thesis. All the simulations performed regarding to a new model proposed by Pirouzpanah et al. [33] which used the Eulerian-Eulerian approach. As a base case model, we considered the pump is working at 60 Hz while the sand diameter and sand density are respectively 53 micrometers and 2300 kg/m³ [33]. Also, the impeller frequency and sand size of 50 Hz and 150 micrometers were used to find their effects on the erosion rate. The pressure at outlet specified as 700 psi and the fluid entered with the flow rate of 2000 bbl/day. The results of these assumptions can be seen in Figs. 12-14. In all the simulations, we presented the pressure contour, velocity profile and erosion rate inside the impeller.

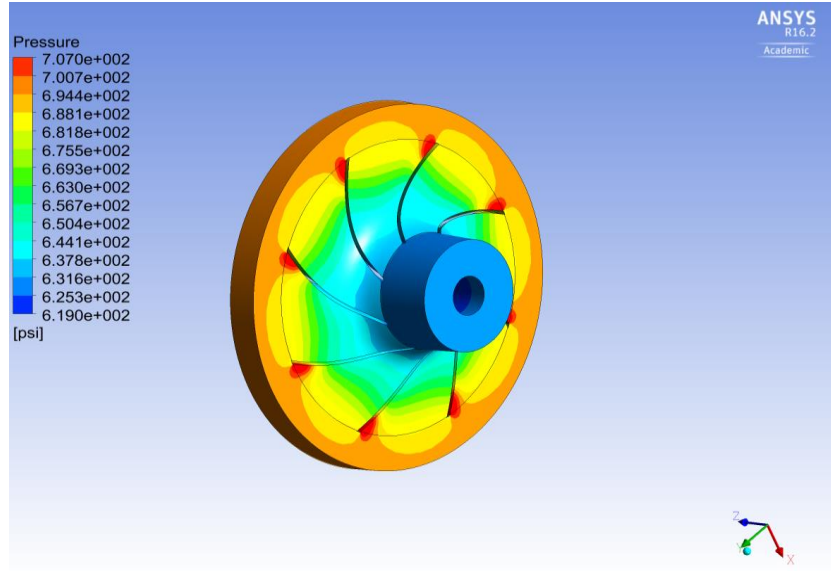


Figure 12. Pressure contour (psia) at 60 Hz, sand size and density as 53 μ m and 2300 kg/m³

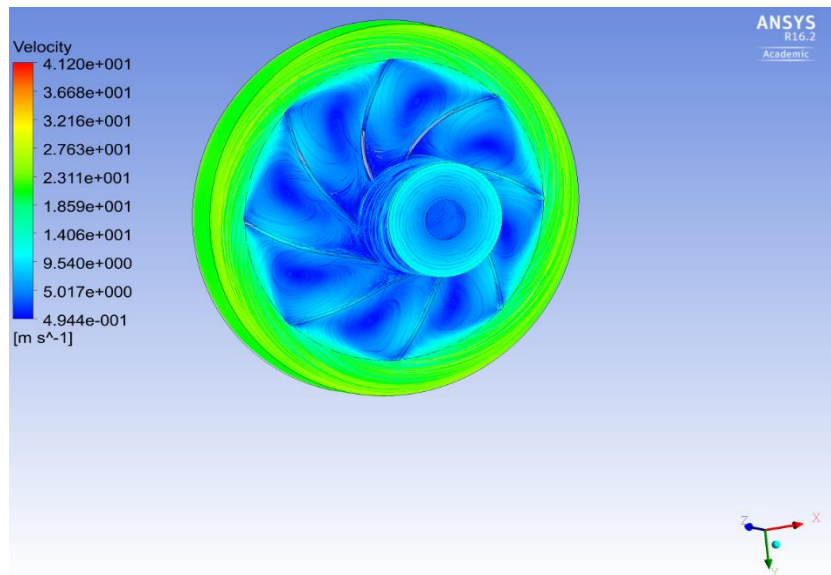


Figure 13. Velocity magnitude (m/s) at 60 Hz, sand size and density as 53 μ m and 2300 kg/m³

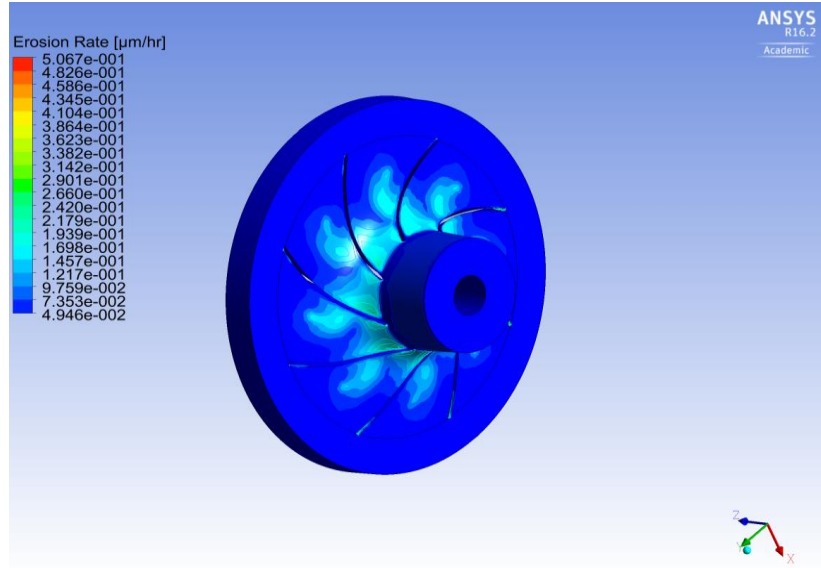


Figure 14. Erosion rate [$\mu\text{m/hr}$] at 60 Hz, sand size and density as $53\mu\text{m}$ and 2300 kg/m^3

Results show that the pump in this condition is capable to increase the total pressure from 616 to 700 psi. Also, the maximum erosion is 5.06×10^{-1} micrometer per hour, which occurs at the entrance of the pump and the leading side of the blades. To find a better pattern about the erosion rate, we investigated other cases in which the parameters such as sand diameter, pressure at outlet, sand density and the rotational speed of the impeller are variable. As a next step, we examined the effect of sand size on erosion rates. For this purpose, the sand diameter changed to 150 micrometers in which all the other assumptions remained fixed. The results of the new case are shown in Figs. 15-17. In the following models, we intended to find the effect of key parameters on erosion rate. Therefore, we compared different scenarios to have a clear insight about the possible ways of erosion rate reduction in ESP. In each of the presented scenarios, one of the major parameters varies while the other conditions and parameters remain unchanged.

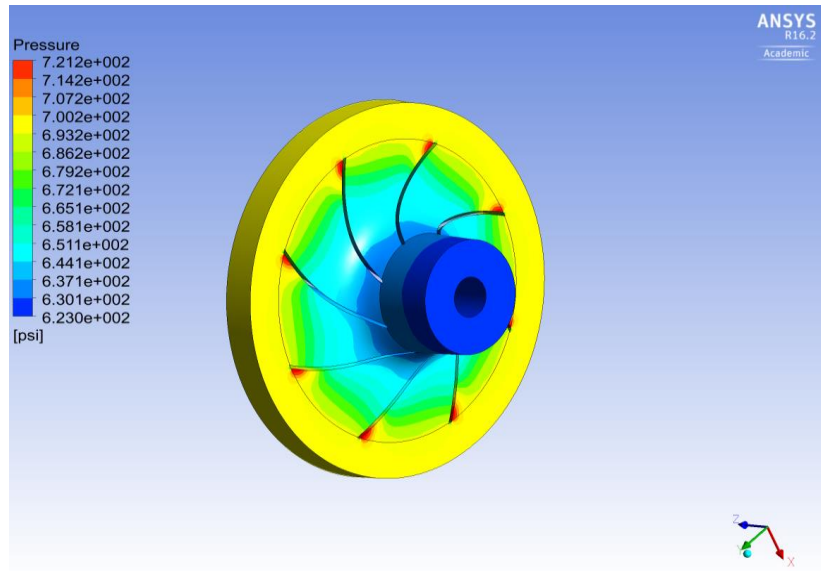


Figure 15. Pressure contour (psia) at 60 Hz, sand size and density as 150 μ m and 2300 kg/m³

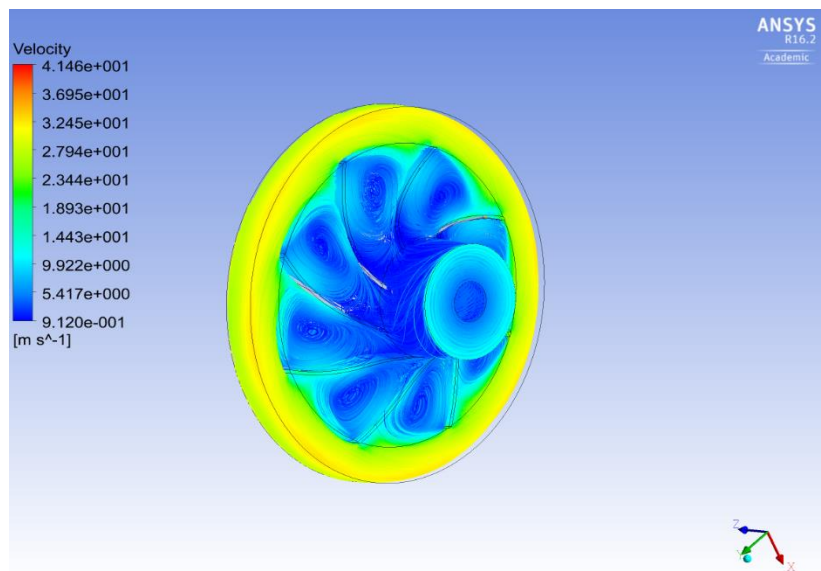


Figure 16. Velocity magnitude (m/s) at 60 Hz, sand size and density as 150 μ m and 2300 kg/m³

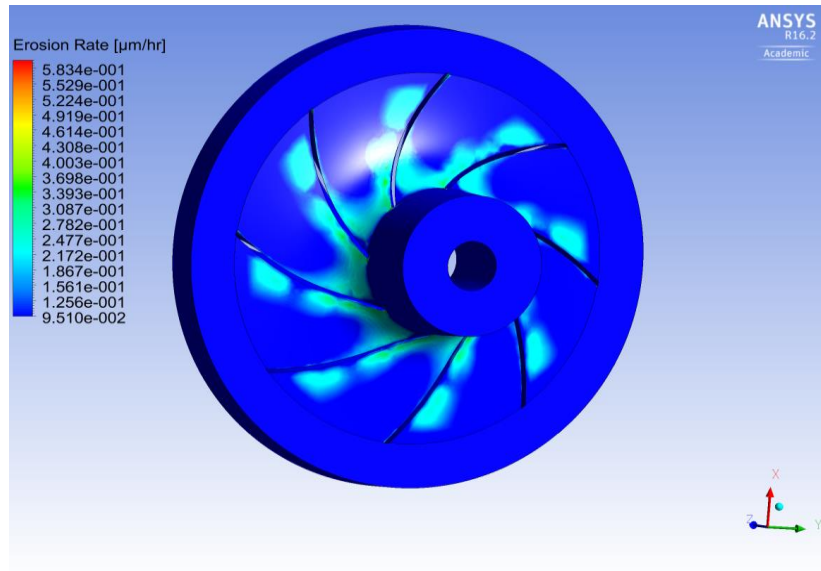


Figure 17. Erosion rate [$\mu\text{m/hr}$] at 60 Hz, sand size and density as $150\mu\text{m}$ and 2300 kg/m^3

In this case an erosion rate increment of 15.1 percent is gained compared to the previous scenario. Also, the erosion is more concentrated on the leading side of the blades which is related to increasing the sand size. In the next scenario we intended to find the effect of rotational speed on erosion rate of the system. So, we kept all the parameters and boundary conditions unchanged except of rotational speed which was set to 50 Hz.

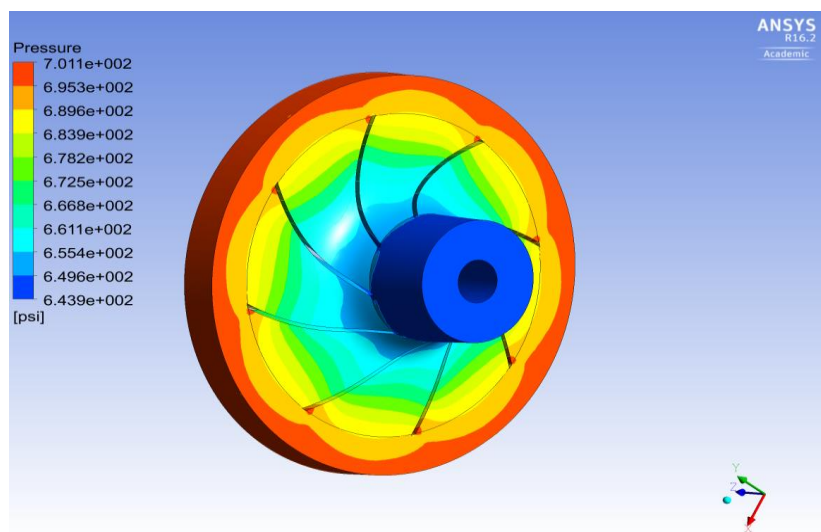


Figure 18. Pressure contour (psia) at 50 Hz, sand size and density as $53\mu\text{m}$ and 2300 kg/m^3

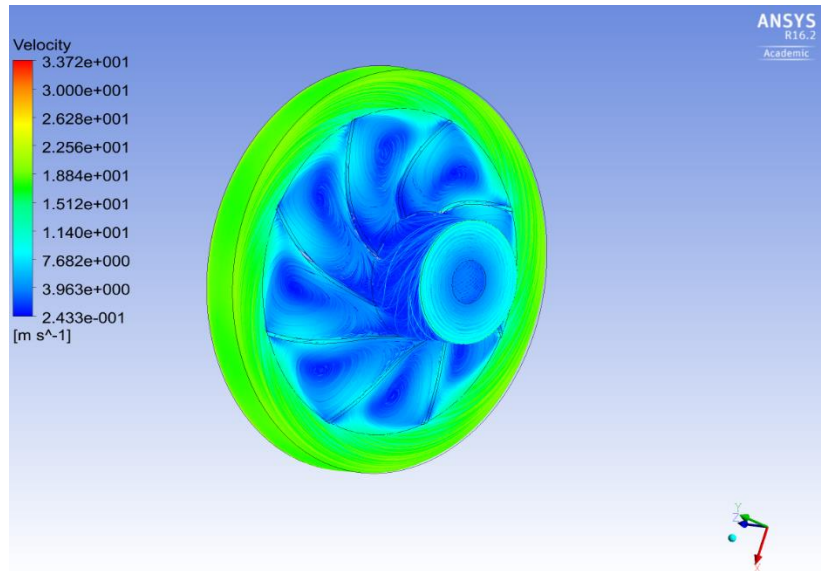


Figure 19. Velocity magnitude (m/s) at 50 Hz, sand size and density as 53 μ m and 2300 kg/m³

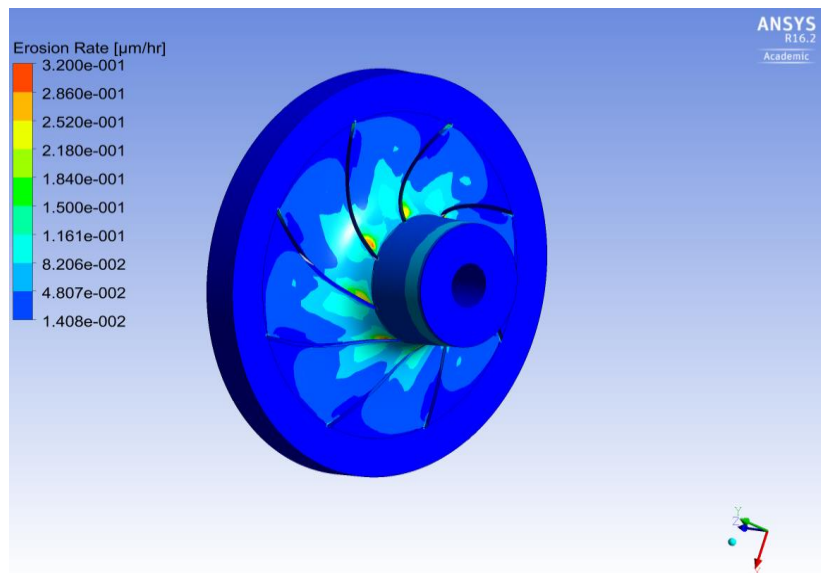


Figure 20. Erosion rate [μ m/hr] at 50 Hz, sand size and density as 53 μ m and 2300 kg/m³

Considering the energy enters to the system by impeller rotational speed, we predicted a farther distance of particle shooting regarding to the higher rotational speed. Taking this into consideration, we can see in Figs. 18-20, the maximum pressure inside the impeller decreases,

besides erosion rate declines by 36.84 percent of its value in the first case. Also, it is obvious in Fig. 20 that the erosion happens more on the inlet of the system, where the system has not enough force to shoot the particles to the farther distances. In addition, the profile of velocity which is in close relationship with the rotational speed is decreased. This means the particles hit the wall by less kinetic energy. To have the effect of both sand size and the rotational speed, we analyzed a model in which the rotational speed is 50 Hz and sand size assumed as 150 micrometers. During the simulation, the rest of the parameters and inputs as pressure output, density and inlet flow rate are constant.

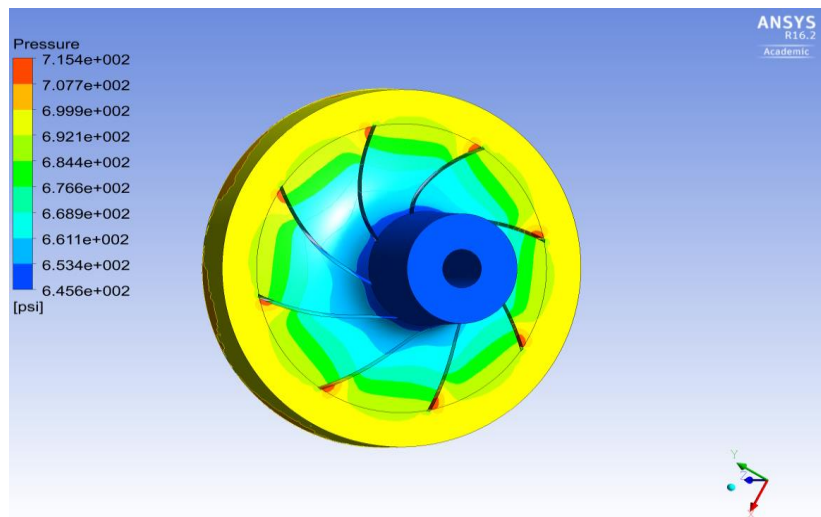


Figure 21. Pressure contour (psia) at 50 Hz, sand size and density as 150 μ m and 2300 kg/m³

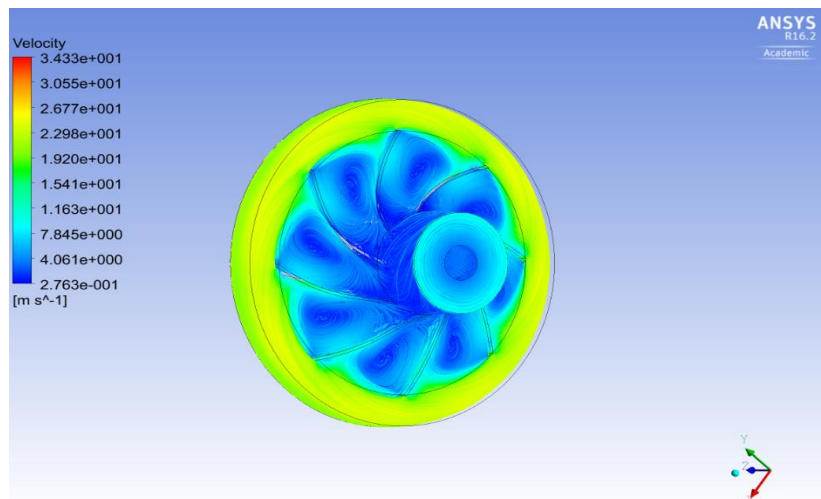


Figure 22. Velocity magnitude (m/s) at 50 Hz, sand size and density as 150 μ m and 2300 kg/m³

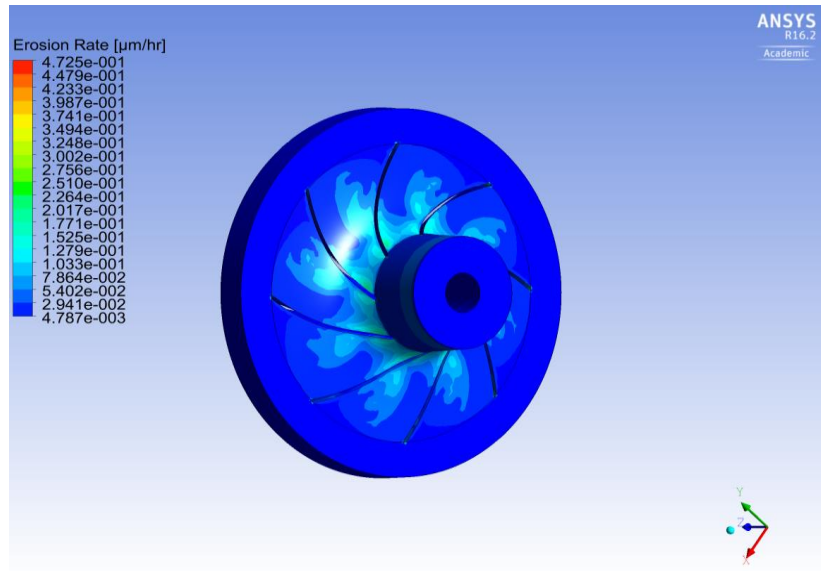


Figure 23. Erosion rate [$\mu\text{m/hr}$] at 50 Hz, sand size and density as $150\mu\text{m}$ and 2300 kg/m^3

In this scenario, total pressure experiences its highest value at the far point of leading edge of the blade, where the last contact between the blade as energy transferor into the system and working fluid happens. In terms of erosion rate, we increased the sand size, whereas the rotational speed is decreased. Based on the previous results, these two parameters have opposite effects on erosion rate. Thus, the net change of erosion rate should be determined proportional to the component that has the dominant impact on it. The results show that the erosion rate is decreased by 6.7 percent compared to the first case study. Also, both the pressure side and leading side of blades are eroded as it can be seen in Fig. 23.

One of the other parameters which has a key impact on the erosion rate is the density of sand particles. Density is related to buoyancy and drag forces on the particles and also indirectly effects on lift force. Therefore, we changed the sand density to 2100kg/m^3 while all the other conditions remained unchanged. That means the system is run by 50 Hz rotational frequency, the outlet pressure set as 700 psi and the mass flow rate at the inlet assumed as 2000 bbl/day.

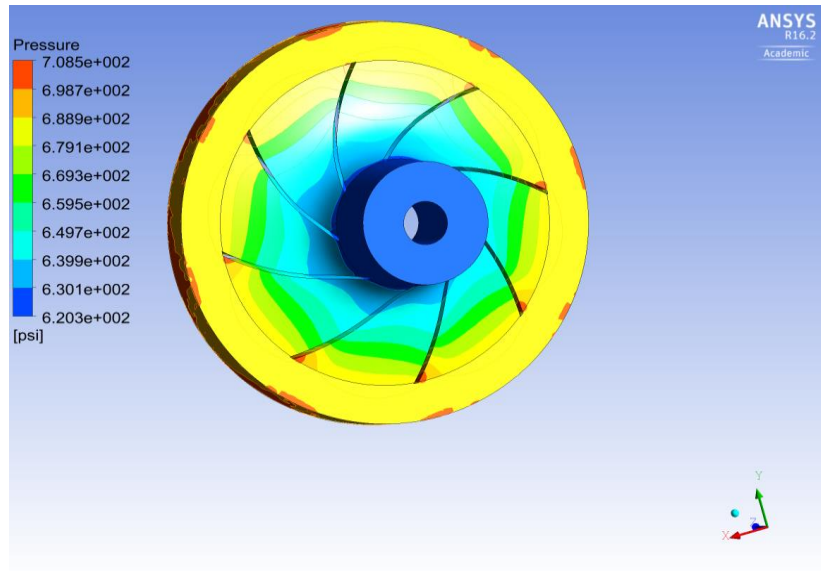


Figure 24. Pressure contour (psia) at 50 Hz, sand size and density as 53 μ m and 2100 kg/m³

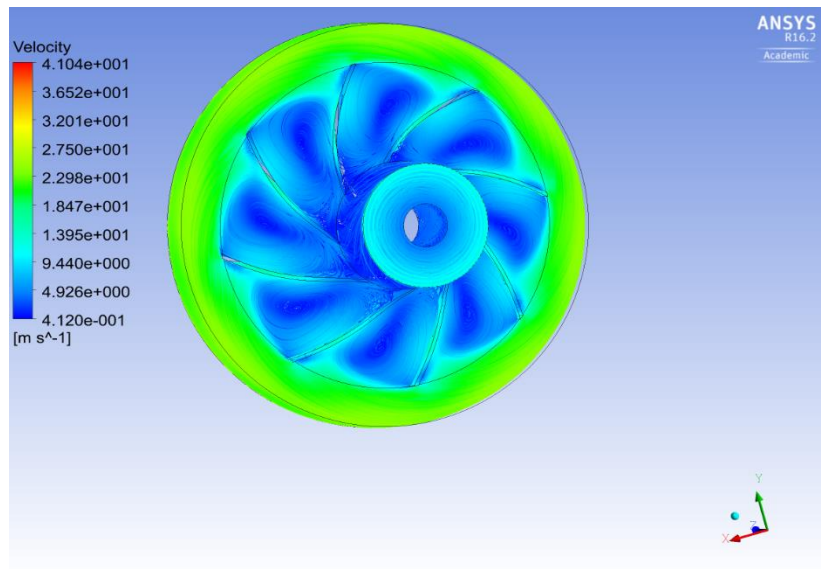


Figure 25. Velocity magnitude at 50 Hz, sand size and density as 53 μ m and 2100 kg/m³

As it can be seen in Figs. 24-26, total pressure increases from 620.3 psia at the inlet to 700 psia at the outlet, which is very close to the base case scenario. It can be concluded that the same level of pressure will be sufficient with the lower frequency of impeller when the particles with lower density enter the system. This conclusion is important, because the rotational speed has a direct

relationship with power consumption of the system. It means that more power saving is expected in this scenario compared to the base case model.

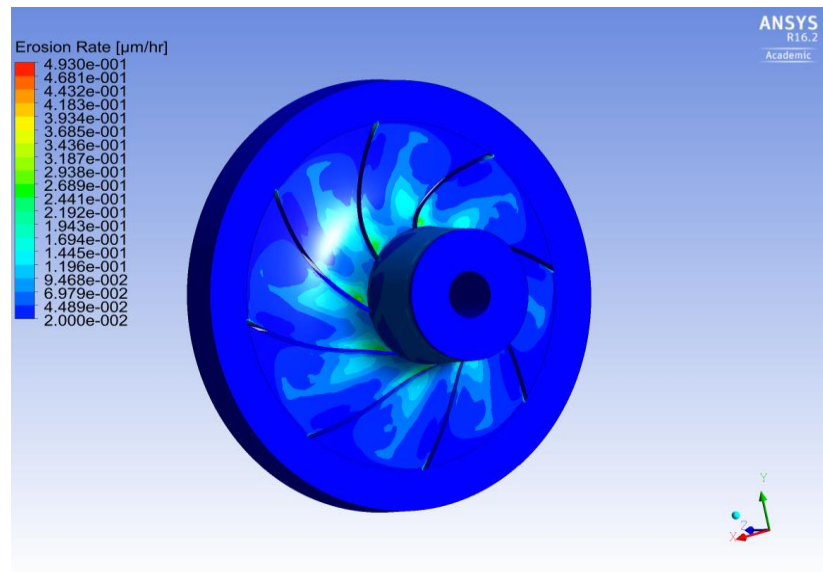


Figure 26. Erosion rate [$\mu\text{m/hr}$] at 50 Hz, sand size and density as $53\mu\text{m}$ and 2100 kg/m^3

In Fig. 26, it can be seen that the erosion rate is decreased from 5.067×10^{-1} in the first case to 4.930×10^{-1} micrometer per hour which is 2.7 percent reduction of the initial value. Indeed, by this system, we can have the same total pressure increase in the system compared to the first case model which conveys the sands with higher density. The other key parameter in erosion rate depends on the working pressure of the system. Once the total pressure increases, it means that the net force on the inlet cross section area will enhance. On the other hand, the acting forces on the particles have the key roles on the erosion rate inside a system based on the previous chapter.

To find the pressure effect on erosion rate, the pressure at the outlet defined as 1000psia, while the other inputs remained unchanged. The results for this case are presented in Figs. 27-29. In this model, impeller rotates at 60 Hz and the sand density and size are 2300 kg/m^3 and 53 micrometers respectively.

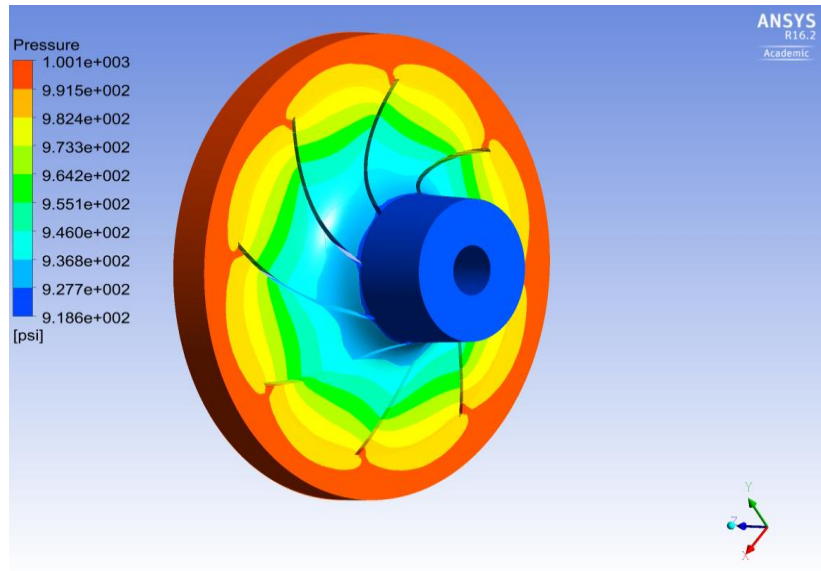


Figure 27. Pressure contour (psia) at 60 Hz, sand size and density as 53 μ m and 2300 kg/m³

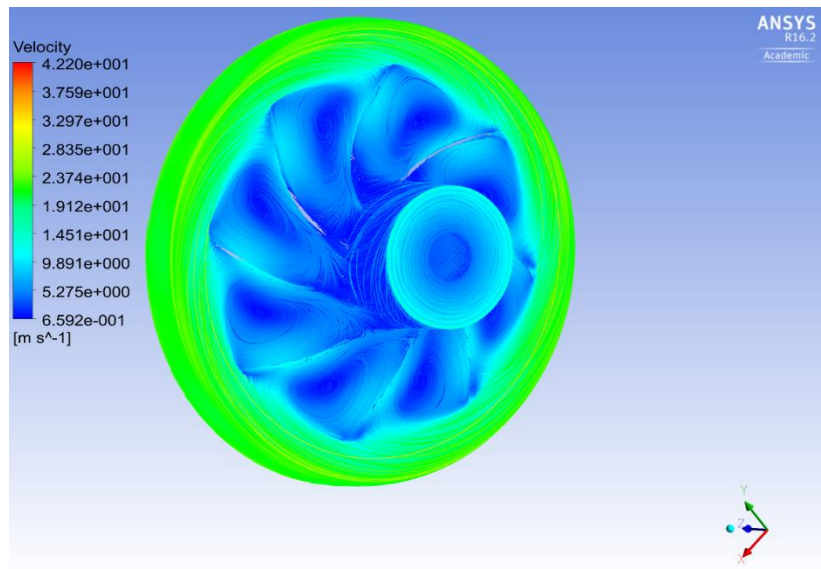


Figure 28. Velocity magnitude at 60 Hz, sand size and density as 53 μ m and 2300 kg/m³

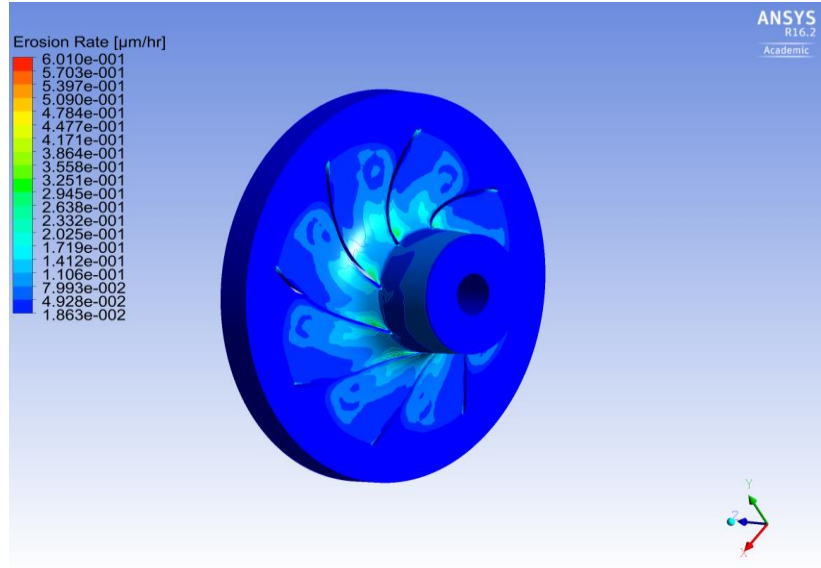


Figure 29. Erosion rate [$\mu\text{m/hr}$] at 60 Hz, sand size and density as $53\mu\text{m}$ and 2300 kg/m^3

Results show that the pump can increase the total pressure by 82.4 psi, also erosion rate experienced higher value between all the case studies. The main could be related to the net force on the particles imposed by the system. Therefore, the particles have enough energy to travel far distances with higher impact on the surfaces. The results demonstrate 18.6 percent enhancement in erosion rate compared to the same system when the pressure at the outlet is 700 psia. Based on the data from the simulation, we can conclude that the working pressure of the pump will have the most effect on the erosion rate. It means that the highest erosion rate would be expected at the last stages of a multistage ESP pump. Also, in terms of increasing the life span of ESP pump, it can be recommended that erosion resistant material coating should be done at the last stages, where the impact of sands is more severe due to the higher working pressure.

In the last scenario, we modeled the impeller with total pressure at outlet as 1000 psia, sand density and size of 2300 kg/m^3 and 150 micrometers and the rotational frequency of 50 Hz. The results for this case can be seen in Figs. 30-33

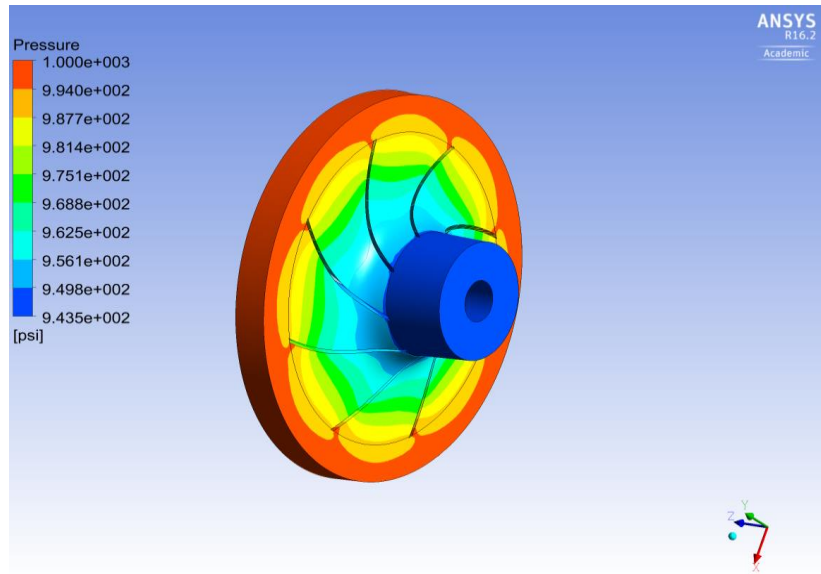


Figure 30. Pressure contour (psia) at 50 Hz, sand size and density as 150 μ m and 2300 kg/m³

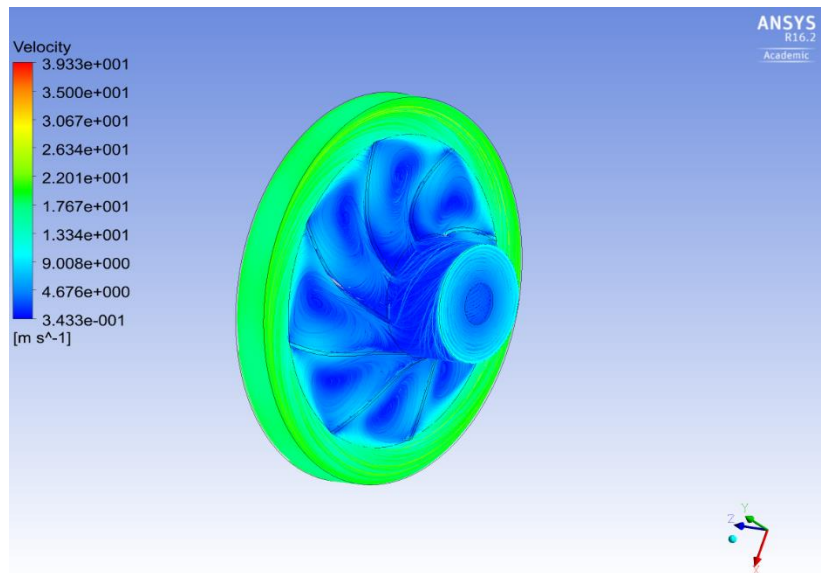


Figure 31. Velocity magnitude at 50 Hz, sand size and density as 150 μ m and 2300 kg/m³

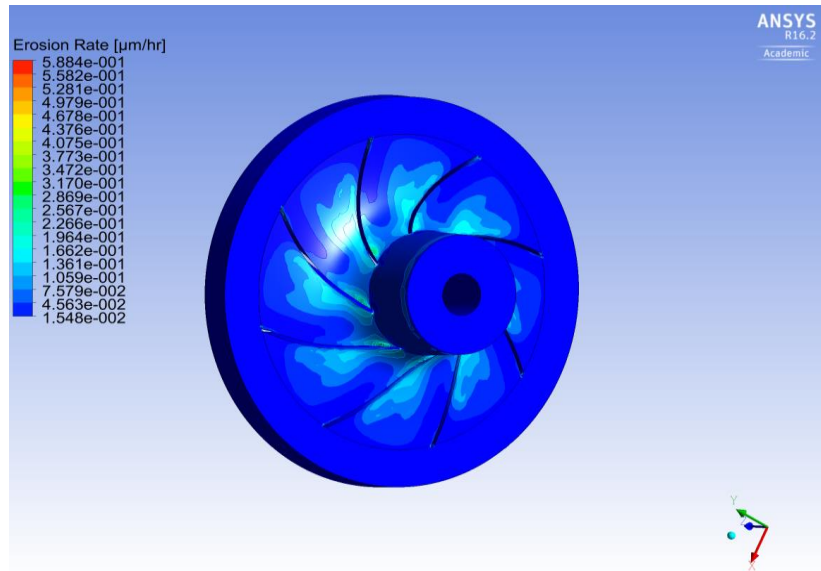


Figure 32. Erosion rate [$\mu\text{m/hr}$] at 50 Hz, sand size and density as $150\mu\text{m}$ and 2300 kg/m^3

Results denote that we can expect pressure increase of 56.5 psi per stage in this case, in which the erosion rate is exceeded by 16.12 percent compared to the first model. Considering last two models with 1000 psia pressure at the outlet, it can be concluded that erosion rate is decreased by 2 percent when impeller is run with lower rotational speed but carries bigger sand size diameter.

CHAPTER V

CONCLUSION AND RECOMMENDATION

CFD simulation for an impeller of an ESP pump is performed with two phase flows where the primary phase was oil and the secondary phase was sand. The model is based on the Eulerian-Eulerian approach and the solving algorithm selected as SIMPLE method. The role of different parameters on the erosion rate was studied, such as sand size, pressure at outlet, rotational speed and sand density. Among all these parameters, the pressure at the outlet shows a significant effect on the erosion rate. Also, the maximum erosion rate usually occurs on the leading edge of the blades where harder material should be used in order to enhance the life span of the pump. Also, the rotational speed can have a major effect on the erosion rate. Hence, we conclude that applying the pump in the lower rotational speed is preferred instead of running at the highest possible rotational speed. On the other hand, if a total pressure is required to carry the oil to the surface, it is better to use more stages to reach to the desired total pressure instead of increasing the rotational speed of the pump.

Since CFD simulation of erosion rate in ESP pump performed successfully, the following studies as the future work are recommended:

- The effect of different working fluid on the erosion can be modeled in the future study. For this purpose, different primary phases can be changed with the same idea of two phase fluid flow or applying the combination of different phases as gas, liquid, and solid to the system. For the later, the effect of different pressures on the phase interchanges can be studied as well.

- The experimental study can be performed to develop the current model of erosion rate.
- The interaction between impeller and diffuser can be obtained by modeling both of them in an ESP pump.
- Different types of erosive materials can be tested for the impeller in order to find their effects.
- In the multistage pump, since the effect of each stage would be important on the next one, the simulation of multistage pump would give a useful information for pump designing.

REFERENCES

- [1] Takacs G. 2009. Electrical Submersible Pumps Manual Design, Operations, and Maintenance, Gulf professional publishing, Elsevier, Oxford, UK.
- [2] Hisham, A.; A. Mubarak Farooq Khan; M. Mehmet OSkay. 2003. ESP failure/Analysis/solution in divided zone-case study, SPE 81488, presented at the SPE 13th Middle East Oil show and conference, Bahrain.
- [3] Clegg, J.D.; S.M. Bucaram; N.W.J. Hein. 1993. Recommendations and Comparisons for Selecting Artificial-Lift Methods, J. Pet. Technol., 45 (12), 1128-1167. SPE-24834-PA.
- [4] Marsis, E.; A. Patill; D. McManus; S. Gray; B. Williams. 2015. A state of the art modeling technique for thrust prediction in bottom hole electrical submersible pumps, SPE 173945-MS, presented at the SPE 13th Artificial lift conference, Brazil.
- [5] Hadjiyannis, S.; N. Charalambous; A. Turlidakis. 2009. An experimental and Computational Study of the Erosion in Submersible Pumps and the Development of A Methodology for Selecting Appropriate Protective Coatings, ASME Turbo Expo, Orlando, Florida.
- [6] Perez, J.; S. Chiva; W. Segala; R. Morales; C. Negro; E. Julia; L. Hernandez. 2010. Performance analysis of flow in an impeller-diffuser centrifugal pumps using CFD: simulation and experimental data comparisons, V European Conference on Computational Fluid Dynamics, Portugal.
- [7] Marsis, E.; R. Russell. 2013. A state of the art computational fluid dynamics simulation for erosion rates prediction in the bottom hole electrical submersible pump, SPE 165452, Presented at the SPE heavy oil conference, Canada.

- [8] Barrios, L.; M.G. Prado. 2011. Experimental visualization of two-phase flow inside an electrical submersible pump stage, *Journal of Energy Resources Technology*, Vol 133 / 042901-1.
- [9] Maitelli, C.W.S. de P.; V.M. de F. Bezerra; W. da Mata. 2010. Simulation of flow in a centrifugal pump of ESP using computational fluid dynamics, *Brazilian journal of Petroleum and Gas*, 4 (1), 001-009.
- [10] Sun, D.; M. Prado. 2003. Single phase model for ESP's head performance, SPE 80925, presented at the 2003 SPE production operation symposium, Oklahoma, USA.
- [11] Pak, E.T.; J. C. Lee. 1998. Performance and Pressure Distribution Changes in a Centrifugal Pump under Two Phase Flow, *Journal of Power and Energy*, 212, 165-171.
- [12] Gonzalez, J.; J. Fernandez; E. Blanco; C. Santolaria. 2002. Numerical Simulation of the Dynamic Effects Due to Impeller-Volute Interaction in a Centrifugal Pump, *Journal of Fluids Engineering, Transactions of the ASME*, 124, 348-355.
- [13] Feng, J.; F.K. Benra; H.J. Dohmen. 2009. Unsteady Flow Visualization at Part-Load Conditions of a Radial Diffuser Pump: by PIV and CFD, *Journal of Visualization*, 12, 65-72.
- [14] Zhou W.; Z. Zhao; T.S. Lee; S.H. Winoto. 2003. Investigation of Flow through Centrifugal Pump Impellers Using Computational Fluid Dynamics, *International Journal of Rotating Machinery*, 9(1), 49–61.
- [15] Asuaje, M.; F. Bakir; S. Kouidri; F. Kenyery; R. Rey. 2005. Numerical Modelization of the Flow in Centrifugal Pump: Volute Influence in Velocity and Pressure Fields, *International Journal of Rotating Machinery*, 3, 244-255.
- [16] Thin, K.; M.M. Khaing; and K.M. Aye. 2008. Design and Performance Analysis of Centrifugal Pump, *World Academy of Science, Engineering and Technology*, 46, 422-429.

- [17] Minggao, T.; Y. Shouqi; L. Houlin; W. Yong; W. Kai. 2010. Numerical Research on Performance Prediction for Centrifugal Pumps, Chinese Journal of mechanical engineering, 23,1-8.
- [18] Zhou, S.; Peiwen Lv; X. Ding; Y. Su; D. Chen. 2012. Numerical Simulation and Impeller Optimization of a Centrifugal Pump, Advanced Materials Research, 472-475: 2195-2198.
- [19] Peri, S.; B. Rogers; M-I Swaco. 2007. Computational Fluid Dynamics (CFD) Erosion study for chokes, SPE 110463, Presented at the 2007 annual technical conference and exhibition, California, USA.
- [20] Sirino, T.; R.E.M. Morales. 2013. Numerical study of the effect of viscosity on an electrical submersible pump, 22nd international congress of Mechanical engineering (COBEM 2013), Brazil.
- [21] Stel, H.; G.D.L. Amaral; C.O.R. Negrao; S. Chivea; V. Estevam; R.E.M. Morales. 2012. Numerical Analysis of the fluid flow in the first stage of a two-stage centrifugal pump with a vaned diffuser, Journal of fluid engineering, 135, 071104-1.
- [22] Muttalli, R.S.; S. Agrawal; H. Warudkar. 2014. CFD simulation of centrifugal pump impeller using Ansys-CFX, International journal of innovative research in science, engineering and technology, 3 (8), 15553- 15561.
- [23] Disting, J.; M. Duporion; F. Monmont. 2014. Improving ESP design through advanced measurement and unsteady simulation of internal flows within stages, SPE 173697-MS, presented at SPE Middle East artificial lift conference, Bahrain.
- [24] Caridad, J.; M. Asuje; F. Kenyery; A. Tremante; O. Aguilon. 2008. Characterization of a centrifugal pump impeller under two-phase flow conditions, Journal of petroleum science and engineering, 63, 18-22.

- [25] Galvao, H.L.C.; G.B.F.F. Oliva; D.P. dos Santos; A.L. Maitelli; R.O. Costa; C.W.S.P. Maitelli. 2015. Computational model of heat transfer in ESP system for deviated wells, SPE 173971-MS, Presented at SPE artificial lift conference, Brazil.
- [26] Bellary, S.H.I.; R. Adhav; M.H. Siddique; B.H. Chon; F. Kenyery; A. Samad. 2016. Application of computational fluid dynamics and surrogate-couples evolutionary computing to enhance centrifugal-pump performance, Engineering application of computational fluid dynamics, 10 (1), 172-182.
- [27] Marsis, E.; S. Pirouzpanah; G. Morrison. 2013. CFD-based design improvement for single-phase and two-phase flows inside an electrical submersible pump, Proceeding of the ASME 2013 fluid engineering division FEDSM 2013, Nevada, USA.
- [28] Syamlal, M.; T.J. O'Brien. 1987. The derivation of a drag coefficient formula from velocity-voidage correlations, Technical Note, U.S. Department of energy, Office of Fossil Energy, NETL, Morgan-town.
- [29] Vakhrushev, A.; M. Wu. 2013. Verification of a discrete phase model with water-particle flow experiments in a tundish, The 5th international conference STEEL SIM 2013, Czech Republic.
- [30] Schiller, L.; Z. Naumann. 1933. Über die grundlegenden Berechnungen bei der Schwerkrafttaufbereitung; Ver. Deut. Ing., 77, 318-320.
- [31] Saffman, P.G. 1965. The lift on a small sphere in a slow shear flow, Journal of Fluid Mechanics, 22: 385.
- [32] Ansys Fluent 12.0 user's Guide, <http://users.ugent.be/~mvbelleg/flug-12-0.pdf>
- [33] Pirouzpanah, S.; G.L. Morrison. 2014. Predictive erosion modeling in an ESP pump, ASME 2014, 4th Joint US-European Fluids Engineering Division Summer Meeting, FEDSM 2014.

Illinois, USA.

[34] Patankar, S.V. 1980. Numerical heat transfer and fluid flow, Hemisphere publishing Co., McGraw Hill, New York, USA.

[35] Nemoda, S.D.; M.R. Mladenovic; J. Paprika; A.M. Eric; D.G. Borislav. 2015. Three phase Eulerian-granular model applied on numerical simulation of non-conventional liquid fuels combustion in a bubbling fluidized bed, Thermal Science, 196-215.